Novel biophysical appliations of STICS

Benoit Vaillancourt
Department of Physics
McGill University
Montréal, Québec
Canada

A Thesis submitted to the
Faculty of Graduate Studies and Research
in partial fulfillment of the requirements for the degree of
Master of Science

Your file Votre référence
ISBN: 978-0-494-66730-9
Our file Notre référence
ISBN: 978-0-494-66730-9

Contents

List of Figures

Abstract

The object of this thesis is to present two novel applications of Spatiotemporal Image Correlation Spectroscopy (STICS) to biological systems. STICS is a technique which uses the correlations in pixel intensity fluctuations of an image time series, captured under fluorescence microscopy, to measure the speed and direction of a flowing population of fluorescently labeled molecules. The method was first applied to measure the dynamics of transport vesicles inside growing pollen tubes of lily flowers. The measured vector maps allowed to confirm the presence of actin filaments along the periphery of the tubes, as well as the presence of a reverse-fountain pattern in the apical region. In a second set of experiments, STICS was used to measure the retrograde flow of filamentous actin in migrating chick DRG neuronal growth cones. These results serve as proof of principle that STICS can be used to probe the response of the growth cone cytoskeleton to external chemical cues.

Résumé

L'objet de cette thèse est de présenter deux nouvelles applications biologiques de la spectroscopie spatio-temporelle par corrélation d'images (STICS). STICS est une technique qui se base sur les fluctuations d'intensité de pixels d'une série d'images de microscopie par fluorescence pour mesurer la vitesse et la direction du mouvement d'une population de molécules fluorescentes. Dans un premier temps, la technique fut utilisée afin de mesurer le mouvement de vésicules l'intérieur de tubes polliniques en croissance. Les champs vectoriels de vélocité ainsi obtenus ont permis de confirmer la présence de filaments d'actine sur la périphérie du tube, en plus du mouvement en entonnoir dans l'apex. STICS fut ensuite utilisé pour mesurer le flux des filaments d'actine l'intérieur de cones de croissance de neurones de ganglions spinaux extraits de poulets. Ces résultats démontrent que cette méthode peur être utlilisée pour étudier les effets de signaux chimiques externes sur la dynamique du cytosquelette de cones de croissance en migration.

Acknowledgments

First and foremost, I would like to thank my supervisor, Prof. Paul W. Wiseman, for giving me the opportunity to experience first hand top-of-the-line research activities. Through all the BBQ's, beer, soccer games, and sometimes research, he has made my stay in his research lab as pleasant as it could have been. I should thank him especially for coping with my last-minute career change, and being supportive all the way to the completion of this thesis.

I want to acknowledge the many collaborators without whom the work presented in this thesis would never have exsited. Prof. Alyson Fournier from the Montreal Neuronogical Institute, and Christopher Kent for providing loads of data for the growth cone measurements. Similarly, I thank Prof. Anja Geitmann from Université de Montréal and Jens Kroeger from McGill University who have allowed me to work with them on the pollen tubes.

I must also take time to thank the members of the Wiseman group, who have all helped me at some point during the last two years: Dave Kolin, the Matlab guru, for helping me with coding and for always knowing how to crack a good joke at group meetings; Elvis Pandzic, the best office mate one could wish for, for providing relief and a good laugh under any circumstances, and for pushing me into joining the soccer team; Jonathan Belisle, for showing me how to use the microsope; and all the other members who know how to laugh and have a good time: Jody Swift, Antoine Godin, Colin Heyes, Alexia Bachir, Jon Comeau, Mikhails Sergeyev, Tim Toplak.

I also thank all the members of Dimensionless: Francis, Phil, Miika and Kevin, for always giving more to look forward to in my small yet meaningful musical career. Rock on.

Closest to my heart is my girlfriend Ming, a model of intelligence, hard work and modesty, without whom the temptation of quitting half-way might have become too strong. She gives me something to look forward to every day, and always succeeds in putting a smile on my face, even without trying. Thank you.

Finally, I thank all members of my family, my brothers Philippe and Matthieu, and especially my parents for all the "coups de pied dans l'cul" they have timely provided from elementary school to this day. They gave me the extra momemtum I needed to make it through the I.B., McGill, and finally through this. More than just food and shelter, they have given me the joy of learning and provided me with more love than I can handle. Merci.

À tout le monde, un gros merci!

Chapter 1

Introduction

All living organisms can be broken down into parts of hierarchical complexity, from molecules, to cells, to organs, to tissues, to systems. The smallest living building block is the cell. Although they are small, cells form a system of extreme complexity where an immense variety of molecules interact to fulfill such roles as transport, migration, and signaling, among many others. While extensive research efforts have unveiled many of the cell's secrets over the past decades, much remains to be done before scientists can claim to fully understand the entire system as a functioning whole.

The approach of molecular biology has long been of establishing causal relationships, which have been used to dress exhaustive tables of molecular pathways within the cell. While such *in vitro* studies are indispensable in creating a framework about the strucutre and functions of cells, the process by which biomolecules act and the dynamic responses in cellular activity *in vivo* are starting to be unveiled as biologists team up with chemists and physicists to study such complex biological systems. Such studies are made possible by inter-field collaborations and the development of novel quantitative techniques at the levels of experiment, data analysis and modeling.

Spatiotemporal image correlation spectroscopy (STICS) is a recently developed fluorescence fluctuation technique which analyzes space-time correlations of image series obtained under fluorescence microscopy [1]. It was developed for biophysical applications, using the correlations in pixel intensity fluctuations to map the movement of fluorescently labeled particles inside living cells [1, 2]. Being a relatively new technique, it has so far been used on only a small number of applications [2, 3]. This work presents two novel applications of STICS on two distinct biological systems. In the first instance, the technique is used to measure the dynamics of transport vesicles inside growing pollen tubes of lily flowers, which is of great interest in understanding

the process by which pollen tubes undergo a particularly rapid growth. The second application is the measurement of actin dynamics inside vertebrate neuronal growth cones, where STICS is used to measure the reponse of cytoskeletal actin to the cone's chemical environment.

This work will first introduce, in Chapter 1, the experimental techniques used and the systems studied. Chapter 2 will introduce the theory behind STICS as an extension of other image correlation techniques. Chapters 3 and 4 outline the experimental details and results of STICS applied respectively to lily pollen tubes and neuronal growth cones. The final chapter summarizes the work and makes suggestions for future investigations.

1.1 Fluorescence Microscopy

When studying cells, it is useful to have at one's disposal an arsenal of minimally-invasive techniques to probe systems *in vivo* without influencing the suctures and dynamics that one is trying to measure (and of course without killing the system). Fluorescence microscopy achieves this by imaging fluorescence emission excited from proteins labeled with fluorescent molecules, which fluoresce when light of a certain wavelength is focused on them. These proteins have revolutionized the field of cell biology ever since the naturally occuring green fluorescent protein (GFP) was first extracted and purified from *Aequorea victoria*, a kind of jellyfish [4]. It is now commonly used as a marker for biological studies.

1.2 Fluorescence

Fluorescene detection is one of the most widely used modalities for quantitative biophysical spectroscopy and microscopy. Fluorescence occurs when an electron in a singlet excited state rapidly returns to the ground state via the emission of a photon of a longer wavelength than that of the photon that was originally absorbed by the molecule to excite the electron [5]. In order to understand the process of fluorescence, one can make use of Jablonski diagrams, named after Alexander Jablonski who introduced the use of such diagrams to represent electronic energy levels [6].

Figure 1.1 shows an example of a Jablonski diagram. The vertical lines show electron transitions between states (only the ground and first electronic states are shown). Excitation via absorption of a photon occurs very quickly, on the order of

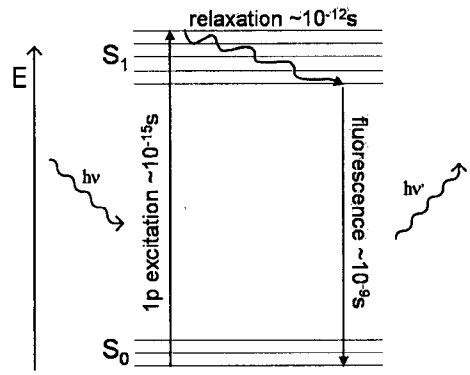

Figure 1.1: An example of a Jablonski diagram. Electrons in singlet electronic states are excited from the ground state (S_o), by the absorption of a photon of energy hν, to a higher electronic state (S_1). A photon of a lower energy hν' is emitted after the electron has lost some energy in vibrational relaxation.

10^{-15} s. Horizontal lines within S_o or S_1 represent vibrational energy levels of the molecule, which quickly relaxes to the lowest vibrational state level in S_1. Vibrational relaxation occurs on time scales of 10^{-12} s, so the lowest vibrational state of S_1 quickly populates. The lifetime in this lowest excited state vibrational energy level is on the order of 1 ns, and subsequent relaxation to the ground state is accompanied by the emission a of fluorescence photon. The frequency ν of the absorbed and emitted photons is directly related to the energy gap E between the ground and excited states, through the simple relation $E = h\nu$.

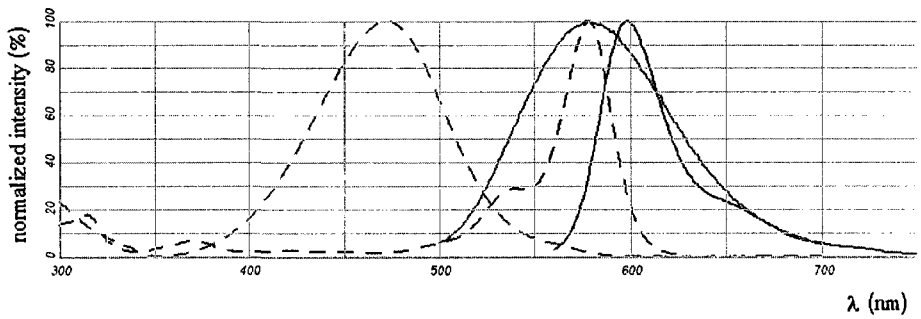

Figure 1.2: Emission (solid) and excitation (dotted) spectra for the fluorescent dyes FM 1-43 (green) and MitoTracker Red (blue), from Invitrogen.

Since excited electrons lose some of their energy through vibrational relaxation,

the absorbed and emitted photons differ slighty in wavelength. This is of great experimental interest, since it allows the simultaneous excitation and detection of a fluorescent sample with the simple use of optical filters to isolate the fluorescence emission. Furthermore, each fluorescent molecule has a unique absorption-emission spectrum, which allows the simultaneous excitation and detection of two (or more) fluorescent populations, given that their emission wavelength peaks are well enough separated in the electromagnetic spectrum (see Figure 1.2). The methods and experiments reported in this thesis were all based on fluorescence detection.

1.3 Transfection Techniques

In order to image proteins in live cells, the fluorescent markers need to be inserted and attached to the desired protein. Many techniques have been developed to achieve this, two of which are discussed in this section. Both techniques require the formation of DNA plasmids, pieces of extra-chromosomal DNA, containing the genetic code for the protein of interest followed by the code for the fluorescent protein marker, say, GFP. Lipofection is the first of these techniques (see Figure 1.3), in which the plasmids are inserted inside a lipid vesicle which can be incorporated inside the cell by endocytosis, which is the process by which the cell membrane surrounds and engulfs outside materials, bringing it into its cytoplasm. When the plasmids enter the cell's nucleus, the new GFP-coding DNA is transcribed and new proteins are produced via the cell's usual machinery for protein synthesis. This results in the cell producing the native protein fused with the fluorescent protein, often producing a perfectly functional protein with a built-in fluorescent marker [7]. Not every combination of protein and fluorescent marker is possible, and control experiments must be made to ensure that cell metabolism and protein function are not affected. Once cells has been transfected, they can be cloned and grown in culture for any subsequent experiment.

One focus of this work is the study of actin dynamics in neurons. Lipofection has a very low efficiency in transfecting neuronal cells [8]; therefore, other transfecting methods must be considered. While more than one method may yield the desired result, this work makes use of recombinant viruses. Viruses have evolved incorporate their own genetic blueprint into the host's DNA and RNA replication systems in order to copy themselves. They are essentially vessels which attach to a cell's outer membrane, injecting their own DNA (or RNA) into the cell, which then blindly creates multiple copies of the virus. The use of recombinant viral vectors for gene transfer

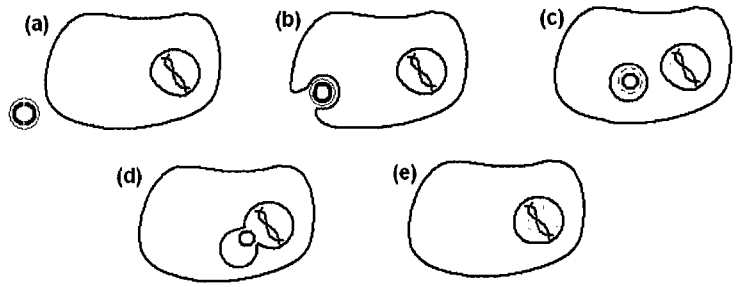

Figure 1.3: (a) A DNA plasmid contains the DNA coding for the fluorescently labeled protein. (b) The plasmid is endocytosed into the cell's cytoplasm where (c) it travels to the nucleus. (d) The vesicle fuses with the nuclear membrane, releasing the plasmid into the nucleus, where (e) it gets incorporated into the cell's DNA.

relies on using a virus' natural function to inject a given DNA plasmid into a cell, thus making the cell synthesize the corresponding fluorescently labeled protein.

The main advantage of these techniques is that once the gene for the fluorescent protein is obtained and successfully inserted inside the cell, one only needs to rely on the cell's native system of enzymes to carry out the transcription, thus making for a cheap and easy way to obtain fluorescently labeled proteins in live cells. Many different colored mutants of the green fluorescent protein, ranging in absorption and emission wavelengths, have been created and can be used to transfect a single cell with two or more fluorophore-coding DNA strands, allowing the simultaneous observation of many different types of proteins by using the appropriate optical filters to image the different emission signals into multiple detection channels.

1.4 Confocal Microscopy

The main idea of confocal microscopy is to only excite fluorophores which lie in the plane of focus, thus allowing to image thin cross-sections of the sample. The schematic in Figure 1.4 shows the main components of a confocal microscope. Light from a laser is scanned across a sample using a set of mirrors. Lenses collimate the beam, which passes through a dichroic mirror before hitting the sample through the objective. The scanning mirrors scan the focal point across the sample, exciting fluorophores across the plane of focus one point at a time. Only the light at the focal point is intense enough to excite the electrons in the fluorescent molecules, thus allowing to excite

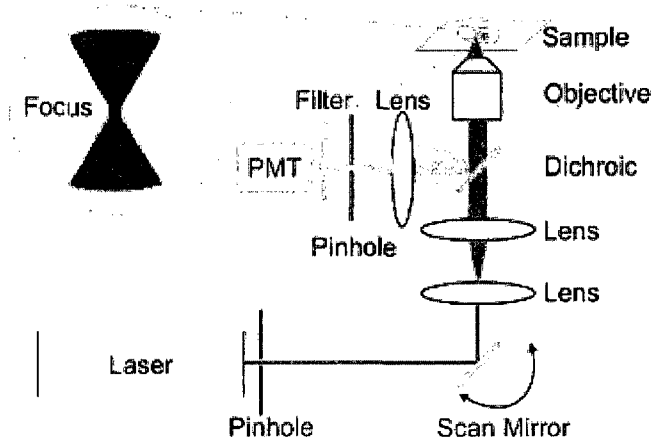

Figure 1.4: Scematic of a confocal laser scanning microscope with epi-detection.

an entire cross-section with limited interference by out-of-focus sample regions. The fluorescence emission, of a higher wavelength than the excitation laser, is reflected by the dichroic mirror into a CCD or PMT. Even though only the molecules along the focal plane are being excited, fluorophores slightly above and below that plane can also be excited and contribute a background glow which reduces the overall signal to noise ratio. In order to limit this effect, a series of pinholes are used. First, the excitation beam is "trimmed" through a pinhole, which reduces the size of the point spread function at the focal point. The emission signal in turn passes through a pinhole, which blocks the out-of-focus compoments along the edge of the beam.

The confocal microscope was invented in 1961 by Marvin Minsky [9]. The application of confocal microscopy to life sciences did not occur immediately for many reasons. First, laser scanning microscopes were only present in physics laboratories, and application to biological sample seemed overly complicated [10]. Second, early techniques relied on moving the whole sample across the focus, which was inappropriate for soft materials and aqueous media typical of biological samples. The first convincing fluorescence images of a biological sample was obtained in 1985 by Brakenhoff and colleagues, and published in Nature [11]. As fluorescence microscopy became the most popular way of studying cells, confocal microscopy was found to be very suitable for eliminating the background glow given off by out-of-focus fluorophores. For a detailed history of confocal microscopy in life sciences, see [10].

1.5 Candidate Biological Systems

The primary advantage of STICS is that it allows to measure the dynamics of fluorescent particles under conditions typically inaccessible to other imagery and image analysis techniques. For example, single particle tracking (SPT) can only be applied when the particle densities are low enough to resolve individual fluorophores and track in time via image time series. This condition is difficult to achieve when a living cell is transfected to synthesize fluorescently labeled proteins, as the expressed protein densities are typically very high at natural expression levels in live cells. This usually implies that intracellular or membrane proteins, when expressed at their normal levels, will not be imaged as individual particles, but rather as an overlapping distribution of the fluorescence signals from different closely packed proteins. Such a system is the perfect candidate for STICS analysis, where the dynamics are measured via the correlated fluctuations of pixel intensities through an image time series, from which the underlying dynamics of the flowing or diffusing populations can be extracted. This section presents the two systems studied in this thesis, while an introduction to the STICS method is deffered until Chapter 2.

1.5.1 Vesicle dynamics in pollen tubes

The dynamics of organelles inside living cells can reveal a lot about their function and interactions. While some organelles are easy to locate and observe using standard microscopy, smaller organelles such as vesicles need more advanced analysis techniques in order to quantify their dynamics. Transport vesicles are small ($\sim$100 nm) "bubbles" made up of a phospholipid bilayer surrounding various materials. They arise from protrusions or invaginations in the membrane of the organelle from which they originate, or from the cell's plasma membrane itself in the case of endocytosis. Similarly, they can fuse with other lipid bilayers, delivering their contents into other organelles or outside of the cell via exocytosis (see Figure 1.5). The concentration of such vesicles can become very high in plant cells that are very metabolically active and ones that undergo constant change of shape or rapid growth. Shape change and growth require the cell's plasma membrane to expand rapidly while forming a cell wall outside the cell surface. The cell wall is a rigid structure which surrounds plant cells and is composed of cellulose and other polysaccharides. An example of such cell activity can be found in the growing tubes of pollen grain cells.

Pollen tubes are long protrusions extending from pollen grains with the function of

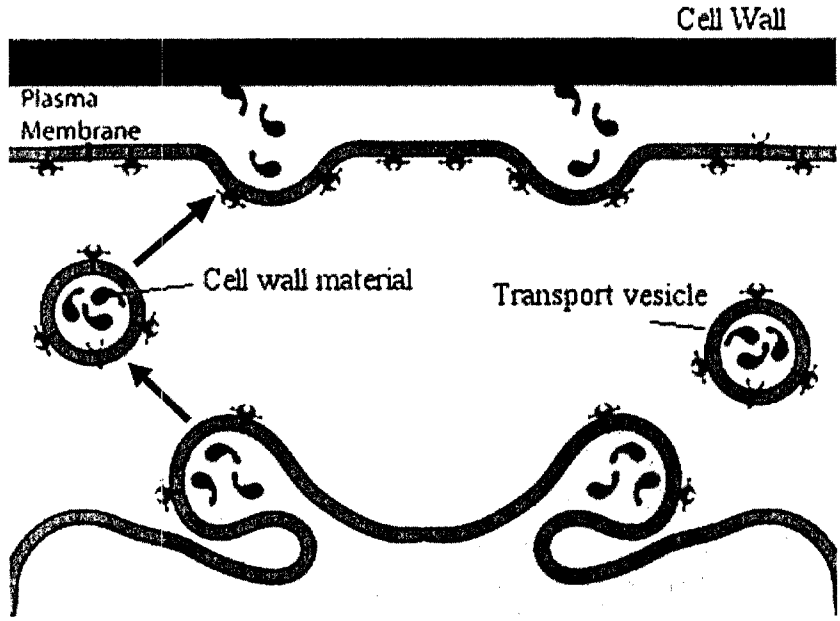

Figure 1.5: Cell wall material produces in intracellular organelles are transported via small vesicles towards the cell plasma membrane. The vesicle's lipid bilayer fuses with the cell membrane, releasing their contents which drive the formation of the exterior cell wall.

delivering the male gametes to the ovules located far down the pistil of the receiving flower [12, 13, 14]. Figure 1.6 illustrates the pollination process for a flowering plant, and the role of pollen tubes in joining the male and female gametes for fertilization. These protrusions can extend very rapidly, reaching speeds on the order of 1 cm/h, a feat that is achieved with the rapid transport of cell wall precursor material, towards the tip of the tube, via small vesicles inside the cell. As mentioned, the vesicles deliver the cell wall material to the outside of the cell by the process of exocytosis. However, in growing pollen tubes they do not randomly fuse with the tube's plasma membrane, but are rather directed rapidly along the tube and towards the apex. [15], where they fuse with the membrane and deliver their material. Such movement happens along actin filaments and microtubules [16, 17, 18, 19], which are arranged in longitudinal cables along the length of the tube as part of the cell's cytoskeleton.

The movement of these vesicles was first decribed by Iwanami in 1956 [20], who observed vesicles moving forward along the periphery of the tube, with a rapid rearward flow down the center. Contrary to larger organelles, transport vesicles enter

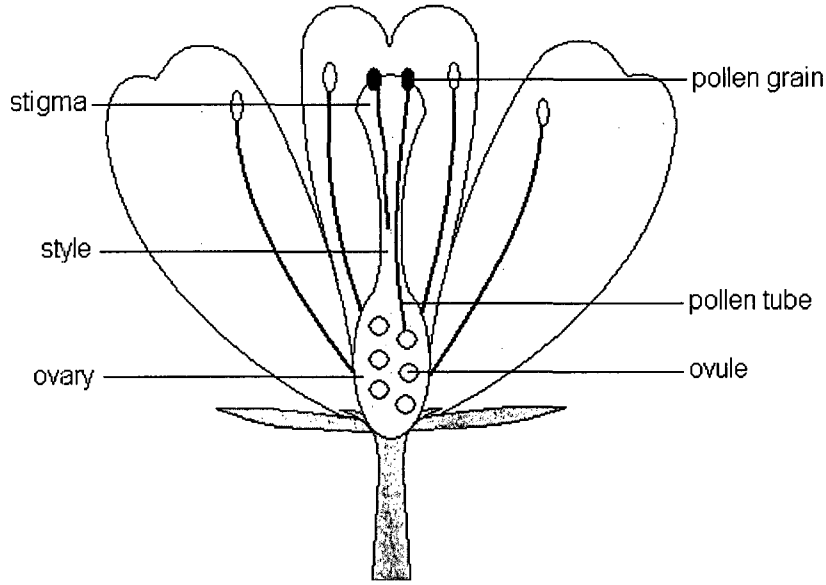

Figure 1.6: A schematic representation of the pollination process. Pollen grains containing the male gametes attach to the stigma. Pollen tubes then extend from the grains and make their way down the style to reach the ovules in the ovary, at the bottom of the pistil (entire light gray area).

deep into the apical region of the tube, reaching the very tip before fusing with the cell membrane [Fig. 1.7]. They enter the apical region by riding along finer actin fibers on the periphery of the cell, a region called the actin fringe [21]. Their movement prior to and after entering the hemisphere-shaped apex is investigated in this work. Prior measurements have been attempted using total internal reflection (TIRF) microscopy, which relies on evanescent excitation, as a means to push the resolution limit [22], but due to the nature of the technique they were limited to a thickness of about 300 nm within the cell membrane, whereas the tubes usually range from 20 to 30 μm in diameter. Vesicles, which range from 75 to 200 nm in diameter, a size below the resolution limit of light or confocal microscopes, are present in large densities, making them a perfect candidate for STICS analysis when imaged in confocal microscopy. The results of the STICS analysis are presented in Chapter 3.

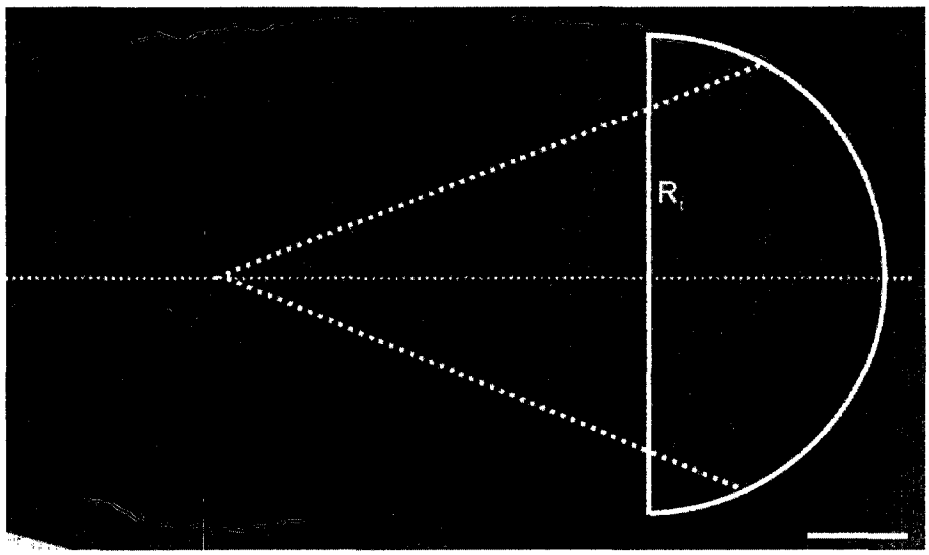

Figure 1.7: Transmission electron micrograph of median section of freeze fixed pollen tube showing the cylinder-hemisphere geometry of the tube, with the vesicles accumulating in a conic section focusing through the center. Ri - radius of the hemisphere shaped apex. Bar = 3 μm. Adapted from [23]

1.5.2 Neuronal growth cones

Nerve cells are very unique in shape and function as they are highly connected with other neurons or muscle cells. They are comprised of a main body, or soma, which contains the nucleus, dendrites and a single long axon which extends outwards from the cell body. Axons are responsible for conducting electrical signals between nerve cells or between neurons and muscles, accomplishing this function through synaptic contacts. Before a synapse is formed, the growing nerve must sense its chemical environment in order to guide its growth towards the correct target. Axon elongation and path finding relies on the growth cone, shown in Figure 1.9: a specialized extension of the cytoplasm at the end of the axon which extends and migrates in response to chemical cues, through active transformations of its actin-rich cytoskeleton. First observed by Harrison in 1910 [24], growth cone structure and function have been extensively studied (for reviews, see [25] and [26]), unravelling some of the molecular pathways driving axon guidance, as well as the cytochemical activity of the cell during the process. However, while biological studies succeed at tracing causal links and dressing intricate tables of molecular pathways, a full understanding of growth cone motility requires a detailed measurement of molecular and neuronal dynamics.

Figure 1.8: A cartoon representation of filamentous F-actin, the polymer of G-actin.

Such highly dynamic activity requires a constant movement and rearrangement of the cytoskeleton, an intracellular network or protein fibers which provides cells with structural support, as well as serving a wide range of functions. Actin is one type of cytoskeleton, and one of the most abundant proteins in eukaryotic cells [27]. First synthesized in 1942 [28], filament actin (F-actin), as found in the cytoskeleton, is composed of actin monomers (G-actin) which polymerize into long (μm scale) filaments (see Figure 1.8).

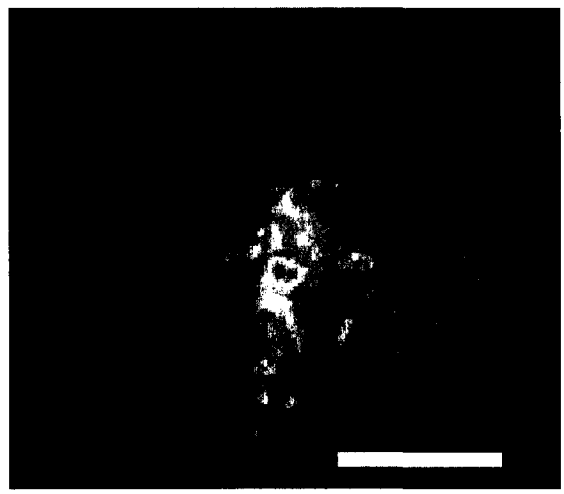

Figure 1.9: A growth cone with fluorescently labeled actin F-actin. The extending filipodia and lamellipodia are faint, with a higher concentration of actin filaments in the central domain. Bar = 10 μm.

Growth cone migration is thought to progress in a process of protrusions and retractions of plasma membrane filipodia and lamellipodia, two structures dominated

by the formation and breakdown of actin filaments [29]. The current understanding is that growth cone motility is mediated by these protrusions, which extend and retract in a random fashion in growth medium, but exhibit a directional bias when subjected to gradients of molecular guidance cues [30]. Many studies on growth cones have concentrated their efforts on the neurons of Aplysia, a type of see slug that has very large (> 100 μm) nerve cells. The study of the Aplysia growth cone cytoskeleton has led to the identification of three major zones [31], shown in Figure 1.10:

1. a microtubule-rich central domain (C);
2. a transitional domain where microtubules and actin filaments overlap (T);
3. an actin-rich peripheral domain (P).

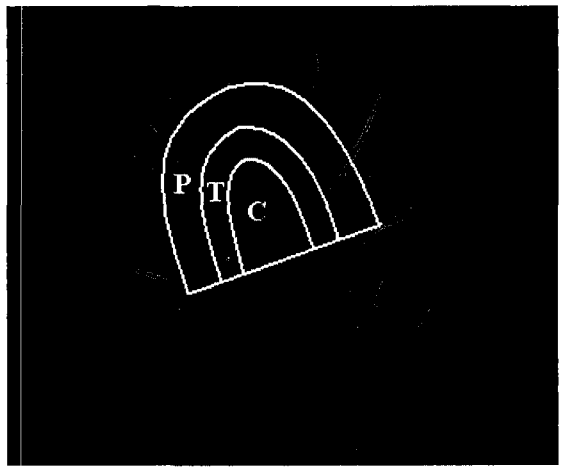

Figure 1.10: Growth cone with fluorescent actin (green) and microtubules (red). The approximate boundaries of the three domains are drawn in white.

Although the three zones can sometimes be considered separately, the underlying cytoskeletal elements are all interconnected. We expect actin dynamics in the cytoskeleton to be affected by external molecular stimuli, and therefore a quantitative study of the movement of filamentous actin (F-actin) in the central domain cytoskeleton could reveal information about the way growth cones respond to their chemical environment. Results of the STICS analysis on chick dorsal root ganglion (DRG) neuronal growth cones are presented in Chapter 4.

Chapter 2

Theory

2.1 Image Correlation Spectroscopy Techniques

Chapter 1 has introduced the systems investigated in this work, as well as the experimental techniques used to study them. Vesicle transport in pollen tubes and actin dynamics in neuronal growth cones are both problems of great biological interest which can be addressed using STICS. In this section, the theoretical and mathematical framework of image correlation spectroscopy methods will be outlined. A brief overview of previous ICS techniques will be followed by a presentation of the theory underlying STICS and a review of the relevant literature. An in-depth review of the advances and applications of image correlation spectroscopy techniques has been published by Kolin *et al* in [32].

Image correlation methods rely on calculating the correlation function of fluorescence intensity fluctuations recorded within an image time series, typically collected using a confocal or total internal reflection (TIRF) microscope. The intensity fluctuations are due to the small size of the diffraction limited focus, the distribution of fluorescent particles in space and the movement of particles into and out of the focal spot (see Figure 2.1). Particles are excited as they diffuse or move through the focal volume, creating a series of images with varying pixel intensities. The fluctuations of each pixel around a mean intensity value can be correlated in either space or time (or both in the case of STICS) and related to physical quantities such as diffusion and flow velocity.

Each image correlation method is characterized by the way they treat the data, either in the temporal or spatial domains, but are similar in that they rely on corre-

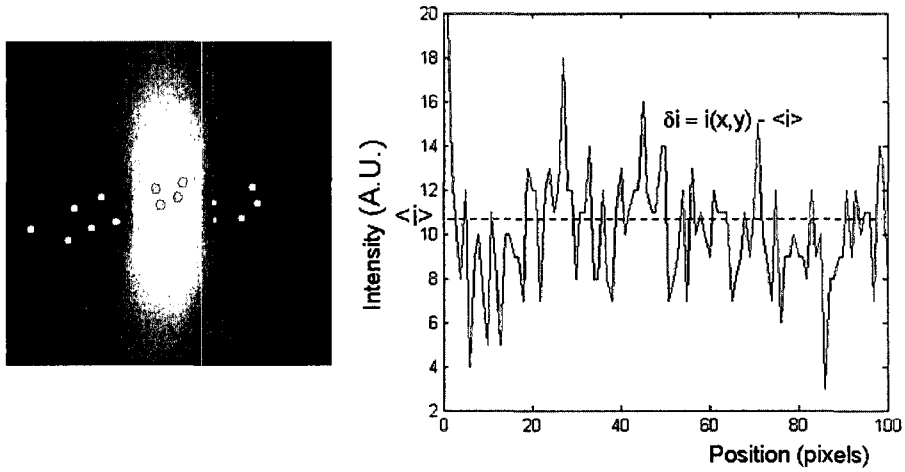

Figure 2.1: A schematic representation of the diffraction limited beam focus. Particles inside the focus emit fluorescence (green), while particles lying outside do not (yellow). The plot shows how the fluorescent signal intensity varies across one line of a single image, as a varying number or particles are excited at each pixel.

lating the intensity fluctuations of the fluorescent signal. As a starting point, we may consider the generalized correlation function [1]:

$$r_{ab}(\xi,\eta,\tau) = \frac{\langle \delta i_a(x,y,t)\delta i_b(x+\xi,y+\eta,t+\tau)\rangle}{\langle i_a(x,y,t)\rangle_t \langle i_b(x,y,t+\tau)\rangle_{t+\tau}}, \tag{2.1}$$

where $\delta i(x,y,t)$ represents the intensity fluctuation of a pixel at position (x,y) for the image recorded at time t, given by:

$$\delta i(x,y,t) = i(x,y,t) - \langle i(x,y,t)\rangle_t, \tag{2.2}$$

where $i(x,y,t)$ is the intensity of the pixel, and the subscripted angular brackets stand for spatial averaging of the frame at time t in the image time series. The angular brackets in the numerator of Eq.2.1 is an ensemble average of pixel intensity fluctuations over all pairs of images separated by τ, with the subscripts a and b representing the general case of signals collected in two detection channels. When $a = b$, Eq.2.1 defines an autocorrelation function, and if $a \neq b$, it defines a 2 channel cross-correlation function.

The image correlation techniques we are concerned with in this thesis rely on making approximations to this general correlation function in order to extract the

desired information.

2.1.1 Image Correlation Spectroscopy

The first application of image correlation spectroscopy (ICS) arose by treating the case $\tau = 0$ in Eq.2.1 above, that is, from the calculation and fitting of the spatial intensity fluctuation autocorrelation function for each frame independently. The technique was used by Petersen *et al* [33] to measure the density distribution of membrane receptors on the surface of live cells. Calculating the zero time lag normalized spatial correlation function for the image recorded at time t,

$$r(\xi, \eta, 0)_t = \frac{\langle \delta i(x, y, t) \delta i(x + \xi, y + \eta, t) \rangle}{\langle i(x, y, t) \rangle_t^2}, \tag{2.3}$$

one obtains a 2D Gaussian function, given that a TEM_{00} Gaussian laser beam was used for excitation. This can be readily fitted as a function of ξ and η, which are the spatial lag (i.e. pixel shift) variables:

$$r(\xi, \eta, 0)_t = \mathbf{g(0, 0, 0)_t} \exp\left(-\frac{\xi^2 + \eta^2}{\omega_o^2}\right) + \mathbf{g_{\infty t}}, \tag{2.4}$$

where the fitting parameters are $g_{\infty t}$, the long-spatial lag offset which accounts for an incomplete decay of the function, $g(0, 0, 0)_t$, the zero-lags peak of the correlation function amplitude, and ω_o, the e^{-2} radius of the Gaussian. For clarity, the fit parameters are highlighted in bold in Eq. 2.4 and every subsequent equation in this section. The peak amplitude $g(0, 0, 0)_t$ is related to the mean number density of independent fluorescent particles within the focal volume [33]:

$$\lim_{\xi \to 0, \eta \to 0, \tau \to 0} r(\xi, \eta, \tau)_t = g(0, 0, 0)_t = \frac{1}{\langle n_p \rangle}. \tag{2.5}$$

Such an approach was also used to measure the changes of platelet-derived growth factor receptor aggregation and density on the surface of live human fibroblasts [33, 34].

2.1.2 Time Image Correlation Spectroscopy

The next approach to ICS is to look at the correlations in the domain separately from the spatial correlations, that is, correlate in time the fluctuations of a single pixel through an image time series, and average in space over multiple pixels. While

spatial ICS can address the question of spatial distribution by looking at fluctuations within a single image, it does not allow one to examine the dynamics of the system at hand. To do so, we must consider Eq.2.1 as a function of time lag τ only, with spatial lag variables ξ and $\eta = 0$:

$$r(0,0,\tau) = \frac{\langle \delta i(x,y,t)\delta i(x,y,t+\tau)\rangle}{\langle i(x,y,t)\rangle_t \langle i(x,y,t+\tau)\rangle_{t_\tau}} \tag{2.6}$$

where the angular brackets denote spatial and temporal averaging. Applying Eq.2.6 to an image time series, we must change τ to a discrete variable measured in terms of the temporal resolution, ultimately an experimental sampling parameter which depends on the microscope system used. In terms of the discrete time lag variable s, Eq.2.6 becomes

$$r(0,0,s) = \frac{1}{N-s}\sum_{t=1}^{N-s} \frac{\langle \delta i(x,y,t)\delta i(x,y,t+s)\rangle}{\langle i(x,y,t)\rangle_c \langle i(x,y,t+s)\rangle_{t+s}}, \tag{2.7}$$

where the angular brackets denote spatial averaging, N is the total number of frames in the image series, and t in this case is a dummy variable for the summation. We should note that the spatial variables x and y, although not explicitely indicated, are also discrete variables and are measured in number of pixels. The resulting function can be fitted with the appropriate analytical model as derived for various type of dynamics. For example, in the case of 2D diffusion with a Gaussian intensity profile focus, the fitting function is [35]

$$r(0,0,\tau) = \mathbf{g(0,0,0)}\left(1+\frac{\tau}{\tau_\mathbf{d}}\right)^{-1} + \mathbf{g}_\infty \tag{2.8}$$

where the fitting parameters are $g(0,0,0)$, the zero-lags amplitude, g_∞, the long-time lag offset and τ_d, the characteristic diffusion time. The τ_d obtained from the fit is related to the diffusion coefficient as

$$D = \frac{\langle \omega_o \rangle}{4\tau_d}, \tag{2.9}$$

where $\langle \omega_o \rangle$ is the mean fit e^{-2} beam focus radius, determined by averaging the e^{-2} radius for the spatial autocorrelation function of every frame.

Similarly, the decay model for the correlation of a sample undergoing directed flow with Gaussian intensity profile illumination is [36]:

$$r(0,0,\tau) = \mathbf{g(0,0,0)} \exp\left[-\left(\frac{\tau}{\tau_\mathbf{f}}\right)^2\right] + \mathbf{g}_\infty \tag{2.10}$$

where the characteristic flow time, τ_f, is obtained from the fit and is used to calculate the flow speed:

$$|v| = \frac{\langle \omega_o \rangle}{\tau_f}. \tag{2.11}$$

Another case of interest to most biological systems is one where the fluorescent population undergoes both diffusion and directed flow, in which case the decay model is simply a combination of Eq. 2.8 and 2.10 above:

$$r(0,0,\tau) = \mathbf{g(0,0,0)} \left(1 + \frac{\tau}{\tau_\mathbf{d}}\right)^{-1} \exp\left[-\left(\frac{\tau}{\tau_\mathbf{f}}\right)^2\right] + \mathbf{g}_\infty. \tag{2.12}$$

This case will be of interest when looking at how the fluctuation correlation functions evolve in time in the case of the STICS method.

2.1.3 Spatiotemporal Image Correlation Spectroscopy

Spatiotemporal image correlation spectroscopy (STICS), which is the focus os this thesis, was developed in 2005 by Hebert [1] as a novel extension of image spectroscopy (ICS) that calculates a full spatio-temporal correlation function of pixel intensity fluctuations recorded in an image time series collected on a fluorescence microscope. The magnitude and direction (i.e. velocity vector) and diffusion coefficient of a population of fluorescent particles can be determined from the evolution of the correlation function as a function of space and time. The method was applied to measure the the directed flow and diffusion of $\alpha 5$ integrin and α-actinin proteins within living CHO cells [1, 2]. It was subsequently used to investigate the linkage of actin and various adhesion-related proteins involved in cell migration [3]. The present work concentrates on further applications of STICS to other biological systems.

Starting from the general spatiotemporal correlation function of Equation 2.1, one can define a discrete approximation to the full function:

$$r'_{ab}(\xi,\eta,s) = \frac{1}{N-s} \times \sum_{t=1}^{N-s} \frac{\langle \delta i_a(x,y,t) \delta i_b(x+\xi, y+\eta, t+s) \rangle}{\langle i_a \rangle_t \langle i_b \rangle_{t+s}}, \tag{2.13}$$

where ξ and η are now discrete spatial lag variables measured in number of pixels,

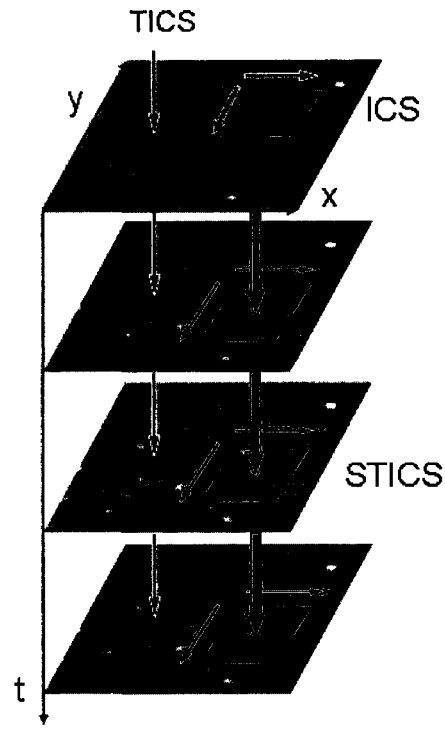

Figure 2.2: The variable domains for respective image correlation techniques. ICS (blue) correlates fluctuations spatially for individual images; TICS (red) correlates fluctuations of individual pixels through time; STICS (green) calculates the fluorescence intensity fluctuation correlations through both space and time.

and s is similarly a discrete time lag representing the number of frames separating the two images being are correlated. Each function is normalized by the spatial average intensity of the images at frames t and $t+s$ respectively, and the calculated functions are averaged over $N - s$ pairs of images within the image time series (for example, within 10 frames, there are 9 pairs of images separated by $s = 1$ frame, 8 pairs separated by $s = 2$ frames, etc.). The correlation functions are typically calculated using Fourier methods to reduce computation time, using a fast Fourier transform to deal with the discrete nature of the function:

$$r(\xi,\eta,s)_t = \frac{FFT^{-1}\left[FFT(i_a(x,y,t))FFT(i_b(x+\xi,y+\eta,t+s))^*\right]}{\langle i_a(x,y,t)\rangle\langle i_b(x,y,t+s)\rangle} \tag{2.14}$$

The first step in the STICS calculation is to compute the $s = 0$ zero-lag autocor-

relation function for each frame, which in essence is no different than spatial ICS, except that the function is averaged over every frame in the movie. The resultant 2D autocorrelation function can be fitted with a 2D Gaussian function. Then the time lag s is successively incremented to measure the average correlation functions of pairs of images throughout the image time series. This results in a series of functions which, when fitted with the appropriate model for diffusion and/or directed flow, can reveal the underlying dynamics of the fluorescent particles.

The basis of this analysis relies on following the evolution of the spatial correlation functions with increasing time lag. The function's peak position will translate from the $(0,0)$ lag position if there is a flowing population, while the time dependent width is an indication of the diffusion coefficient. The functions are fitted to a 2D Gaussian of the form:

$$r'_{ab}(\xi,\eta,s) = \mathbf{g_{ab}(0,0,s)} \exp\left(-\frac{(\xi-\mathbf{x(s)})^2+(\eta-\mathbf{y(s)})^2}{\mathbf{\omega_{o,ab}}^2}\right) + \mathbf{g_{\infty ab}(s)} \qquad (2.15)$$

where $g_{ab}(0,0,s)$ is the central amplitude peak, $x(s)$ and $y(s)$ are the x and y coordinates of the peak's position, $\omega_{o,ab}$ is the e^{-2} waist radius and the $g_{\infty ab}$ is the long spatial lag offset of the correlation function with time lag $\Delta t = s\ \delta t$, where δt is the time between frames. This fitting for increasing s of a free moving Gaussian allows accurate tracking of the time evolution of the spatial correlations present in the pixel fluctuations of the image time series. For example, a directed flow will result in the correlation peak's position shifting proportionaly to the flow speed and direction. Several different cases are shown in Fig. 2.3 for computer simulated image series. Once we have extracted the peak's position coordinates, $x(s)$ and $y(s)$, the speed and direction of the flow are readily calculated:

$$\begin{aligned} x(\Delta t) &= -v_x \Delta t \\ y(\Delta t) &= -v_y \Delta t, \end{aligned} \qquad (2.16)$$

which yields a complete velocity vector (v_x, v_y), allowing one to measure the flow of particles in a given sample. The negative sign in Eq. 2.16 simply comes from the order in which each pair of images are correlated in Eq. 2.14, where we multiply the FFT of the first image with the complex conjugate FFT of the second one, thus

introducing the negative sign in the calculation.

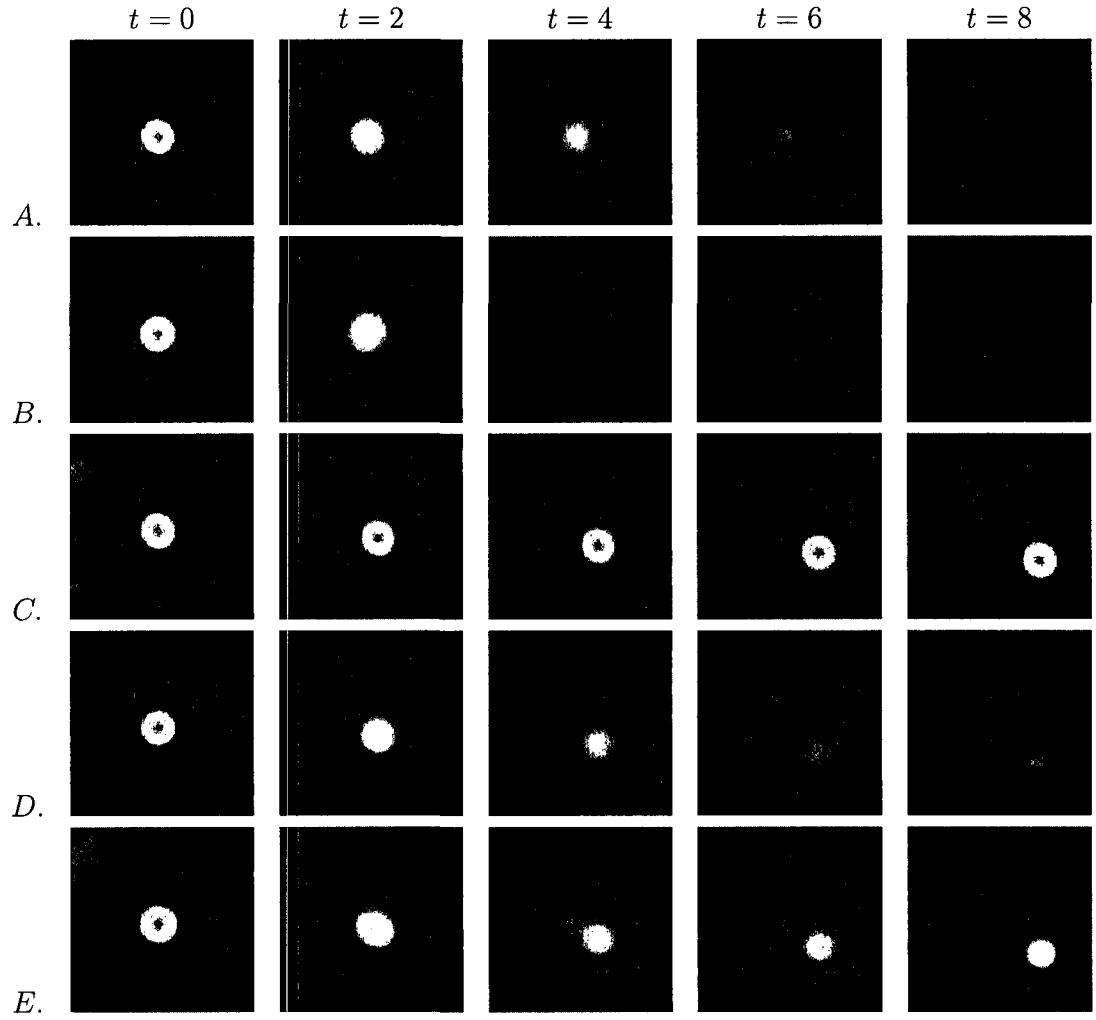

Figure 2.3: STICS calculations made over simulated image series for various dynamics. A: Random diffusion. B: Flow of a constant magnitude for particles moving randomly. C: Directed flow shows the peak moving steadily in the direction opposite to the flow. D: Directed flow combined with some random diffusion shows the peak moving and broadening. E: Two populations, one randomly diffusing and one undergoing directed flow. Adapted from [2].

Immobile Population Removal

The presence of an immobile or slowly moving population in a sample will introduce strong correlations at $(0, 0)$ lags, making it difficult to track the peak of the correlation

function corresponding to the flowing population, especially at early time lags. Since the moving particles in biological systems often make up only a fraction of the total fluorescent signal, their correlation peak for small time lags will be buried under the correlation due to the static component centered at $(0,0)$. Two approaches have been developed to address this problem [2]. The first one aims at removing the DC component of every pixel's intensity time trace through filtering in Fourier space. This is done prior to the STICS analysis, where the corrected pixel intensities are given by:

$$i'_a(x,y,t) = F_f^{-1}\left\{F_t\left((i_a(x,y,t))\right) \times H_{\frac{1}{T}}(f)\right\} \tag{2.17}$$

where T is the total time of the image time series, F_t is the Fourier transform with respect to time, F_f^{-1} the inverse Fourier transform with respect to the pixel fluctuation frquency f, and $H_{\frac{1}{T}}(f)$ is the Heavyside function which is zero for $f < 1/T$ and equals 1 for $f \geqslant 1/T$. Thus we define the slow moving or immobile population as the component which does not fluctuate over the time scale of the entire series, and impose a cutoff in frequency to remove this component and calculate the correcte intensities.

The Fourier filtering approach described above works well for subtracting the immobile population from each image; however, a diffusing population also contributes greatly to the correlation function without showing as a DC component in individual pixels' time traces, thus masking the flow correlation peak. One way to remove this slowly diffusing population is to apply a windowed average filter, where we subtract, from each frame in the image time series, the average intensity over a time window of a certain duration centered on that frame. The corrected pixel intensities are then given by:

$$i'_a(x,y,s) = i_a(x,y,s) - \left[\frac{1}{2\Delta N+1}\sum_{n=s-\Delta N}^{s+\Delta N} i_a(x,y,n)\right] + \langle i_a(x,y,s)\rangle_t \tag{2.18}$$

where for each frame s, we subtract the average intensity calculated over a time window of size $2\Delta N + 1$. The third term is added to prevent Eq. 2.1 from diverging when calculating the autocorrelation functions.

Experimental Considerations

The advantages of STICS for measuring flow vectors have already been briefly discussed. It allows the measurement of dynamics of particles which are too small to be resolved and tracked individually, if their density is too high. With the addition of immobile component filtering algorithms, it can accurately measure the flow speed with up to 90 % of the signal coming from the immobile components [1]. This makes it a powerful tool for measuring the movement of various membrane proteins in cells.

The accuracy and precision of spatial ICS and TICS were investigated by Costantino *et al* [37] and Kolin *et al* [38], in which they found that the most important factor in density measurement was the spatial sampling, taking a 16x16 pixels^2 area as the smallest usable region for sufficient averaging of the correlation function. In STICS, the same limit applies in the calculation of the correlation functions, but the spatial sampling also imposes an upper limit to the velocities that can be extracted from the calculation, because the correlation peak amplitude must be tracked for a time lag of at least one frame. In terms of velocity vector components, the maximum speed which can be measured along any axis is given by [2]:

$$v_{\max\, x(y)} = \frac{N_{x(y)} \times \Delta x}{2 \times \Delta t}, \tag{2.19}$$

where $N_{x(y)}$ is the subregion size in pixels, Δx is the spatial resolution in μm per pixel, and Δt is the time resolution in sframe. Since one usually wishes to reduce the subregion size to the minimum 16x16 pixels^2 in order to appoach cell edges, the time resolution must be made short enough to be on the same scale as the characteristic flow time. For example, in the case of actin dynamics in growth cones, using 16x16 pixels^2 subregions with 0.2μm pixel size and about 3 seconds per frame, the maximum velocity that can be measured is approximately 0.5μm/s, which is faster than the typical speeds in F-actin retrograde flow ($\sim$ 0.1μms). On the other hand, vesicle transport in pollen tubes reaches much higher speeds, and therefore requires a much faster imaging system in order to reduce the time resolution, using a fast 10 framess camera to probe speeds up to 1.3μms ($v_{\max} = 11\mu$ms).

The effect of noise on STICS measurement was investigated in [2]. STICS was proven to perform very well under low signal to noise (SN) ratios, accurately recovering the flow speeds in computer simulated image time series with low SN (standard deviation of the noise equal to signal amplitude), particle densities as low as 0.1 particle per beam focus area, and a time sampling of 10 frames. The experimental

conditions encountered in this work are well above this threshold, so STICS can be applied with confidance without consideration of noise effects.

Example calculation

The image time series are analyzed using a STICS software written in Matlab by David Kolin of the Wiseman lab. The software contains a graphical interface in which the analysis parameters are set, the image series is displayed and the results are shown. The experimental parameters to set are:

- Size of analysis subregion (pixels): the size over which the correlation functions are calculated, typically 16 or 32 pixels.
- Subregion spacing (pixels): the distance between the analysis subregions. Subregions overlap if the spacing is less than the subregion size.
- Maximum time lag (frames): the maximum τ value over which fluctuations are correlated. The calculation ends before this value if the beam radius or the correlation local maxima thresholds are reached.
- Immobile removal type: Fourier, moving average, or none. The type of immobile removal is determined by experiment for each image time series.
- Beam radius threshold (microns): the maximum e^{-1} waist radius allowed for the correlation functions. If the correlation function waist radius exceeds the size of the diffraction limited Gaussian point spread function, the analysis stops for the given subregion.
- Correlation local maxima: the ratio of the noise correlation peak amplitudes to the amplitude of the fluctuation signal correlation function. Analysis is aborted if the noise correlation peaks are large compared to correlation function (typically 0.5).
- Vector mismatch threshold: since the analysis subregions typically overlap, the measured velocity vectors are not independent from each other. This threshold filters out vectors which deviate by a certain amount with respect to their neighbours.

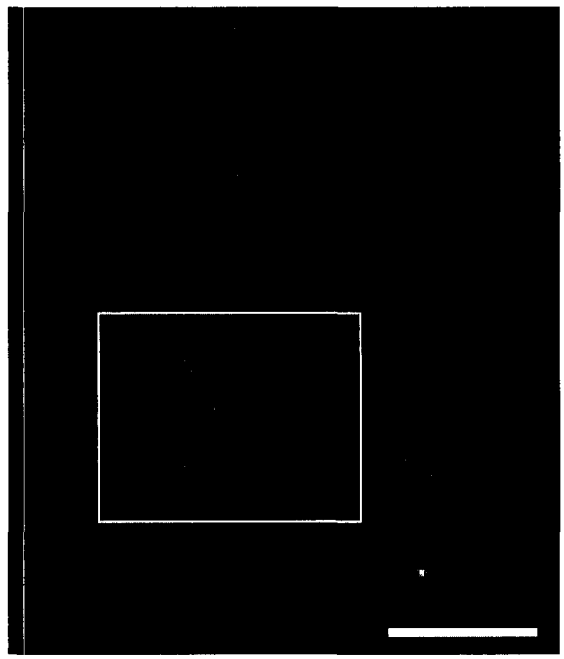

Figure 2.4: A growth cone imaged under wide field microscopy. The images are cropped around the growth to be analyzed with STICS. Bar = 15 μm.

A sample image time series of a growth cone, shown in Figure 2.4, is used here as an example to show the details of the STICS measurement. The images are first cropped around the growth cone for better visibility, before being loaded into Matlab. The image time series is opened with the STICS software, together with the imaging parameters (spatial and time resolution) and the analysis parameters described above. The analysis subregions are set to a size of 16x16 pixels^2, 4 pixels apart. Typically, the beam radius threshold is set to 0.8 μm, equivalent to 4 pixels for a 0.2 μm pixel size, which means that the analysis will stop for a given subregion if the correlation function exceeds are total width (diameter) of about 8 pixels. The correlation local maxima threshold is typically set to 0.5 to ensure that local noise correlation peaks do not disrupt the correlation functions.

The image time series in cropped in time to select the appropriate number of frames for the analysis. It is important to choose a time window over which the movement within individual subregions is constant, to get an accurate averaging of the correlation functions. The immobile filtering algorithm is then applied to the cropped series. The region of interest (ROI), shown in Figure 2.5, is determined, and

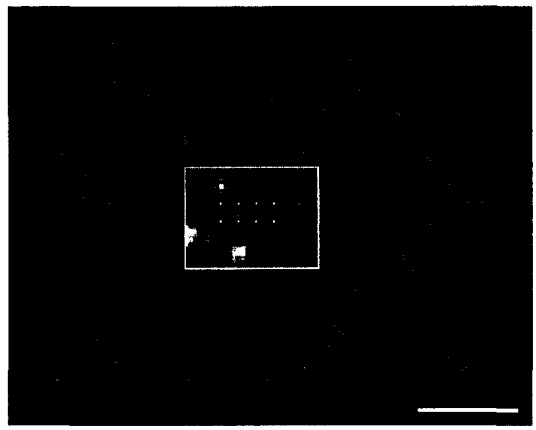

Figure 2.5: The ROI is delimited by the white box. The area is divided into a mosaic of 16x16 overlapping regions, indicated with a white dot in their center. Bar = 5 μm.

the software automatically marks the maximum number of 16x16 subregions which can fit 4 pixels apart within the ROI. The center of these subregions is indicated with a dot in Figure 2.5. The STICS algorithm then calculates the correlation functions for pairs of frames separated by τ, with $0 \leqslant \tau \leqslant$ N, where N is the number of frames kept in the temporal crop (20 in this case). However, the analysis will typically end before reaching the maximum time lag if the beam radius or the local correlation maxima thresholds are exceeded. The result of the STICS measurement on the ROI shown in Figure 2.5 is shown in Figure 2.6.

Each velocity vector in Figure 2.6 is obtained by tracking the correlation function amplitude peak for increasing time lag. For example, Figure 2.7 shows the evolution of the correlation function for one analysis subregion (one vector) of the generated vector map. The calculation goes up to $\tau = 6$ frames, after which it was stopped because it exceeded one of the fit thresholds.

Recall that the vector calculated from STICS is opposite in direction to the translation of the correlation function, because of the complex conjugate in Eq. 2.14. For the example of Figure 2.7, the peak's position for time lag $\tau = 14.5$ s (6 frames at 2.42 seconds per frame) is (0,-0.9) μm away from the center, which yields an average speed of 0.062μm/s, or 3.72μm/min. The velocity values obtained in the STICS algorithm are calculated by a linear regression on the peak's position with respect to time lag.

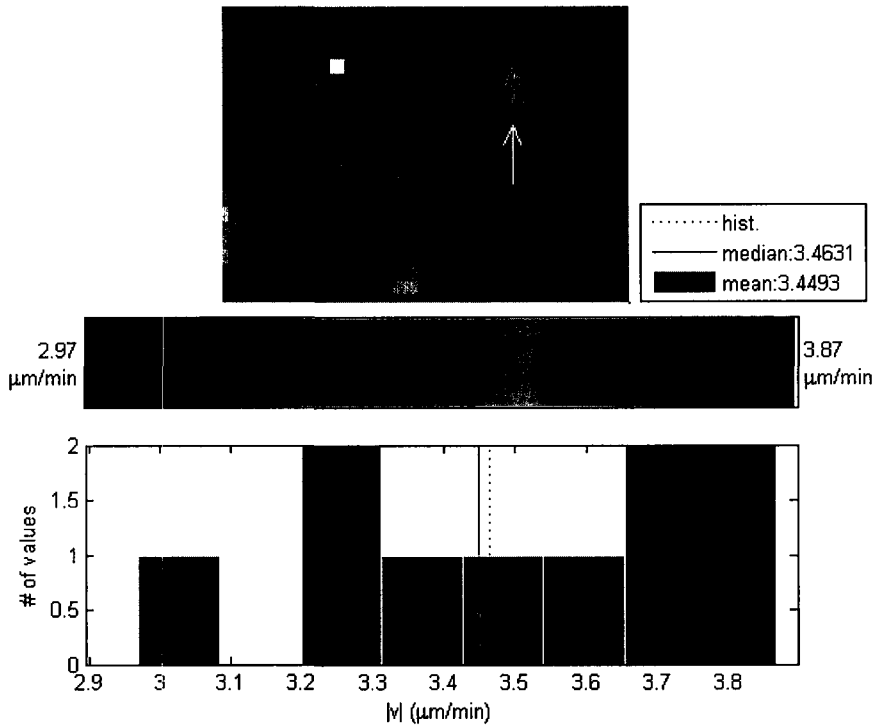

Figure 2.6: STICS measurement on the F-actin retrograde flow of a neuronal growth cone. An average speed of ~ 3.4 μm/min is measured. Pixel size: 0.22 μm

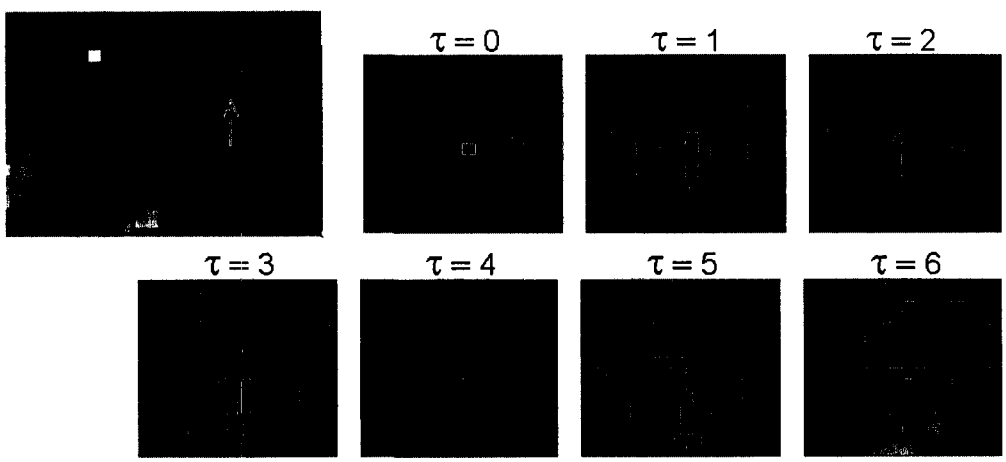

Figure 2.7: The evolution of the correlation function is shown for the vector calculated from the region highlighted in green. τ is given in number of frames, with 2.42 seconds per frame.

Chapter 3

Vesicle dynamics in pollen tubes

STICS was applied to measure the dynamics of transport vesicles in growing pollen tubes of lily flowers. As discussed in the introductory chapter, pollen tubes are long protrusions which extend from pollen grains and travel down through a flower's pistil, to reach the ovules and allow fertilization. They are highly dynamic systems, with rapid dynamics of internal transport vesicles which move towards, and fuse with, the tip of the tube to allow the extension of its membrane and push the growth forward. In this chapter, the experimental details are presented, followed by the results and a discussion of the STICS analysis performed by the author.

3.1 Materials and Methods

The biological experiments and imaging in this section were performed by Jérôme Bové in Anja Geitmann's lab at the Université de Montréal, and STICS analysis was performed by Benoit Vailancourt. Pollen grains of *Lilium longiflorum* were harvested from Anja Geitmann's laboratory at the Montreal Botanical Garden, in affiliation with Université de Montréal. The grains were stored overnight in gelatin capsules on silica gel at -80°C. The pollen was then rehydrated for 30 min in a humid chamber and transferred to a germination medium containing 1 nM KNO_3, 130 nM $CA(NO_3)_2$, 160 nM H_3BO_3, 10 % sucrose and 5 mM MES buffer adjusted to pH 5.5. The image time series analyzed in this chapter were generated by the Geitmann lab, but a discussion of the experimental procedure is outlined in this section for completeness.

In order to study vesicle dynamics in the growing tubes, the lipophilic fluorescent dye FM 1-43 (Molecular Probes, Invitrogen) was added to the germination medium.

The dye was quickly internalized, and after 5 minutes the pollen tubes were washed and resuspended in germination medium, diluted with a solution of 1 % melted low gelling temperature agarose type VII (Sigma) and immediately transferred to the microscope slide. By staining for this short period of time, the dye is allowed to be internalized and bind to the highly dynamic vesicles, without having time to diffuse to other organelles such as mitochondria, as will be shown below.

The imaging was done on a Zeiss LSM 510 META / LSM 5 LIVE / Axiovert 200M system. The microscope was mounted with with a Plan Apochromat 100x/1.4 N.A. oil differential interference contrast (DIC) objective. Image acquisition was done in LIVE imaging with excitation via a 488 nm diode laser at 100 mW excitation power and fluorescence emission collected with a 550 nm long pass filter. Images of 512x512 pixels^2 were recorded, with a pixel size of 0.14 μm/pixel and temporal resolution of 0.107 s/frame.

3.2 Results

A control experiment was conducted prior to data analysis to ensure that the movements recorded with microscopy imaging corresponded to vesicles, and that other cellular organelles did not influence the measurement. The FM 1-43 dye will bind to phospholipid bilayer membranes which also surrounds organelles such as mitochondria, and therefore the staining may not be selective for the vesicles. The control was done by labeling mitochondria with the fluorescent dye MitoTracker Red CMXRos (Molecular Probes, Invitrogen) which was added to the germination medium after the FM 1-43 labeling and washing steps. Figure 3.1 shows the control fluorescene images clearly showing the accumulation of the FM 1-43 label in the apical region where the vesicles are located, with the MitoTracker being confined to the shank of the tube. We also notice little or no colocalization between the two signals. The mitochondria are the organelles, in addition to the vesicles, which reach furthest into the apex of the tube [39], so the control is a clear indication that only the vesicles are labeled by the FM 1-43 dye.

The application of STICS to pollen tubes is very similar to the example from growth cones shown in Chapter 2 (see Figures 2.6 and2.7). An example of the correlation function evolution for increasing time lags is shown in Figure 3.2. The correlation function's peak is located by a 2D Gaussian fit, and the velocity vectors are extracted by fitting the peak's position in x and y with increasing time lag.

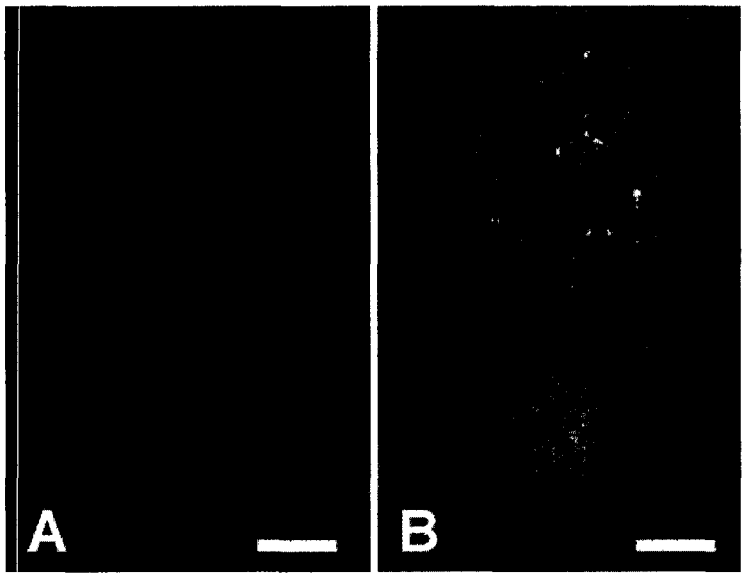

Figure 3.1: Control experiment for FM 1-43 dye labeling. A: Fluorescence micrograph of a pollen tube labeled with FM 1-43 fluorescent dye. The high intensity in the apical region indicates that the dye is bound to vesicles that are concentrated there. B: Fluorescence micrograph superimposed with the corresponding DIC and fluorescence images of mitochondria labeled with MitoTracker Red. The absence of colocalization of the green and red dyes confirms that only the vesiles are labeled with FM 1-43. Bar = 5 μm. From [23] with permission.

Four image time series were analyzed using the STICS software. By varying the analysis parameters, we can probe different processes of vesicle dynamics, depending on their spatial range and charactistic flow times. Figure 3.3 shows two vector maps of vesicle movement calculated over subregions of 32x32 pixels with 8 pixel spacing, correlated over 100 frames in time. The vector maps revealed a rearward movement through the center of the tube with speeds up to 84 μm/min (1.4 μm/s). It important to note that both figures were calculated using the same parameters, with the region of interest (ROI) in Fig. 3.3(B) extending further towards the tip of the tube where the flow is faster, thus making the slower movements more difficult to see, because the color legend is rescaled for every map.

In Fig. 3.3(A), the turning of vesicles from the forward movement in the periphery to the rearwards central flow is clearly seen. The movement in the apical region, however, is smeared out due to the shorter range spatial correlations of the flow in that region. Indeed, if the movement is not uniform, the entire set of movements across

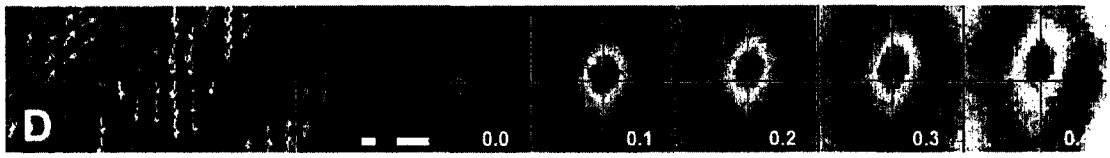

Figure 3.2: Example of STICS applied to pollen tube vesicle dynamics. The vector marked with a magenta dot on the left panel is derived from fitting in time the position of the 2D correlation function's peak, shown on the right for increasing time lags. The correlation functions are averaged through an image times series of 100 frames, and calculated over 32x32 pixels^2 subregions. Scale bars = 1 μm. From [23], with persmission.

a subregion of analysis may not be spatially correlated, making the STICS analysis inaccurate or impossible to interpret (see Fig.2.3). Furthermore, by averaging the fluctuation correlation functions over 100 frames, the average may not converge to a resolvable Gaussian function, since the correlated movement of frames separated by the same time lag s may differ greatly between the first $1 + s$ and the last $N - s$ frames of the series.

In order to probe the short range dynamics of the vesicles in the apical region, the analysis subregions were reduced to 16x16 pixels in size. At the same time, this allowed us to apply the analysis slightly closer to the edge of the tube, revealing details of vesicle movement as they approach or leave the tip for material delivery. The images are correlated over 50 frames, which allows a good averaging of the correlation functions. The functions can typically be tracked for $5 < \tau < 25$ frames, before they leave the analysis subregion or the peak becomes becomes buried in noise floor due to the lack of long time lag correlations in the movement and amplitude decay due to coupled diffusive movements.

Fig. 3.4 shows STICS vector maps of vesicle movement in the apex of the tube. It is interesting to note that the flow is not uniform across the inverted cone that is seen on the fluorescence images, where the vesicles form a reverse fountain shape, flowing forward along the periphery before reaching the tip and turning rearwards down the center. Instead, vesicles seem to move somewhat randomly in this region, which explains why many subregions do not yield a clear flow vector when analyzed by STICS. The flow is also slower, reaching speeds of about 0.7 μm/s, about half of the highest velocities measure in the shank of the tube.

A second example is shown in Figure 3.5, where similar movements are observed

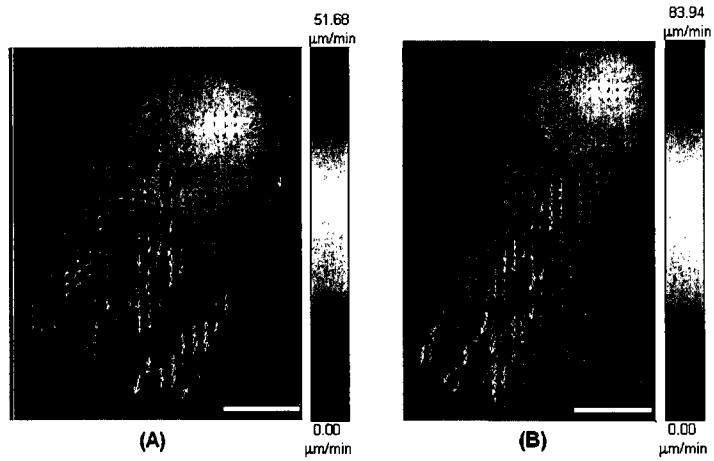

Figure 3.3: (A) STICS generated vector map of vesicle dynamics calculated over 32x32 pixel subregions with 8 pixel spacing, correlated over 100 images in time. The turning movement of vesicles from forward to rearward flow is clearly seen on the left side of the tube. Some retrograde movement is also observed in the apical region. (B) The same vector map as (A), with the ROI extended into the shank to show the accelerating movement of vesicles down the center of the tube. Bars = 10 μm.

in the apex of the tube, although with a more uniform pattern. The vesicle dynamics in this tube exhibit similar features. Although the reverse fountain movement is more evident, there is some degree of randomness in the movements. The vector magnitudes are consistent with the other 4 tubes that were analyzed at various times (data not shown), with speeds ranging mainly between 0.3 and 0.5 μm/s. Forward movement along the periphery is very clear, consistent with the model of an actin fringe leading up to, but not into the apical region (see discussion). In fact, studies of the cytoskeleton reveal that the actin filaments do not extend into the apex [21], instead releasing the vesicles at the subapical boundary, at which point vesicle movement is dominated by hydrodynamic forces.

3.3 Discussion

As mentioned above, the observed dynamics of transport vesicles in growing pollen tubes agrees with the notion that vesicles are transported along the actin filaments of the cytoskeleton running parallel to the axis of the tube. The turning observed at the subapical boundary (see Figs. 3.3, 3.4 and 3.5) also indicates that the actin

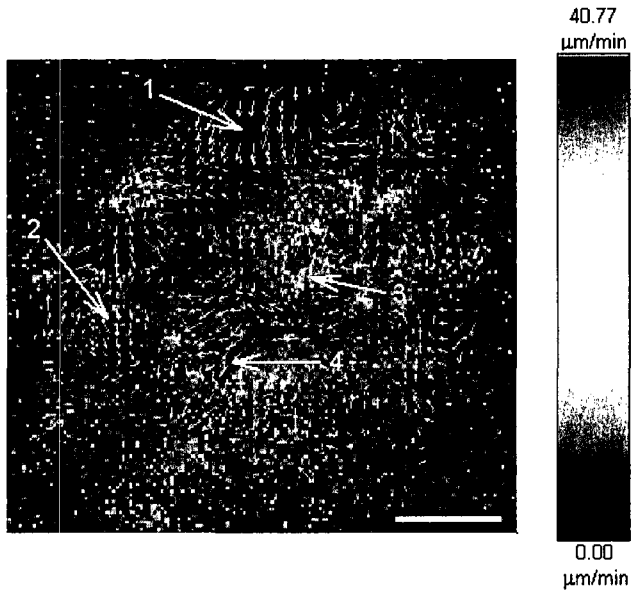

Figure 3.4: STICS generated vector map generated over the apical region of the tube portrayed in Fig. 3.3, with analysis subregions reduced to 16x16 pixels with 4 pixel spacing, correlated over 50 frames. High speed retrograde movement of vesicles after delivery is seen at the tip (1), as well as some turning from from the periphery to the inverted cone of rearward flow (2). Some forward flow is seen (3), as well as the rearward central flow (4). Bar = 10 μm.

filaments penetrate furthest around the periphery, without entering the hemisphere-shaped apex, forming the actin fringe reported by Lovy-Wheeler [21]. The retrograde flow in the apex, converging towards the center in an inverted cone, together with the observed turning, indicates that not all vesicles succeed in contacting and fusing with the plasma membrane, but are rather taken by the rearward stream, to be recirculated at a later time.

A series of fluorescence recovery after photobleaching (FRAP) experiments were conducted by Anja Geitmann's lab as a part of this work [23]. In FRAP, the fluorescent particles are bleached over a region of the sample, and the rate at which the fluorescence intensity is recovered across ther region is interpreted as the rate of lateral diffusion of the labeled species [40]. It can also be used to reveal qualitative information about the directed movement of the fluorescently labeled molecules. The results shown here in Figure 3.6 are consistent with the STICS analysis, showing the recovery of fluorescence starting around the shoulder of the tube and turning towards

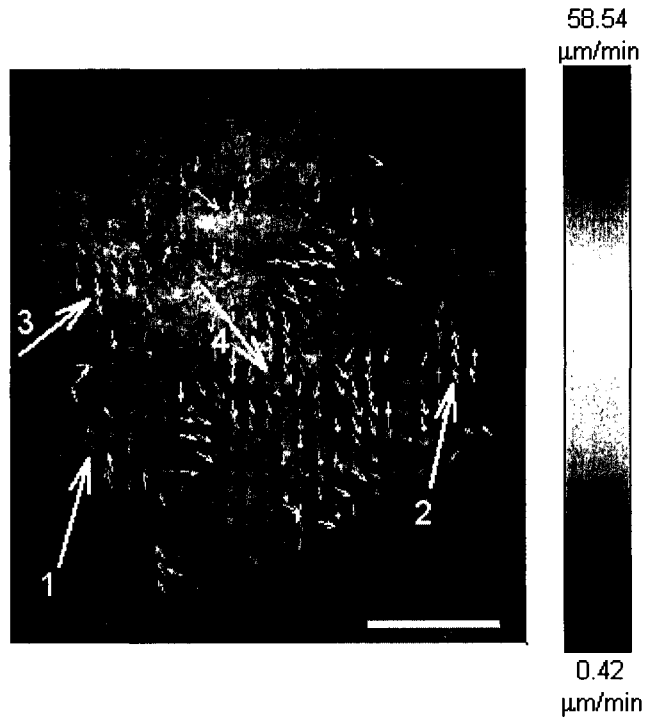

Figure 3.5: STICS generated vector map of vesicle movement in the apex of a pollen tube, calculated over 16x16 pixels subregions. Peripheral movement along the actin fringe is clearly seen (1 and 2), while the rearward flow following delivery is consistant from the tip (3) towards the center (4). Bar = 10 μm.

the center, forming the reverse fountain flow to finally fill in the hemispherical tip. This indicates that the release of material and fusion of vesicles with the plasma membrane happens along the edges of the apical region, as they are released from the actin fringe, and not at the very end. It also confirms the role of vesicles as the source of material for plasma membrane extension during tube growth.

Bové *et al* [23] also used a simple model to calculate the amount of material required to expand the plasma membrane during sustained growth. The problem of material requirement arises from the fact that each vesicle, by releasing material and fusing with the plasma membrane in exocytosis, contribute a larger volume to the outside cell wall than they contribue surface area to the plasma membrane since the volume of a vesicle (i.e. the amount of material inside) scales as R^3 while the membrane surface area scaled as R^2, where R is the vesicle radius. By using a radius of 8.3μm for the hemisphere shaped apex, a cell wall of 170 nm thickness and a tube

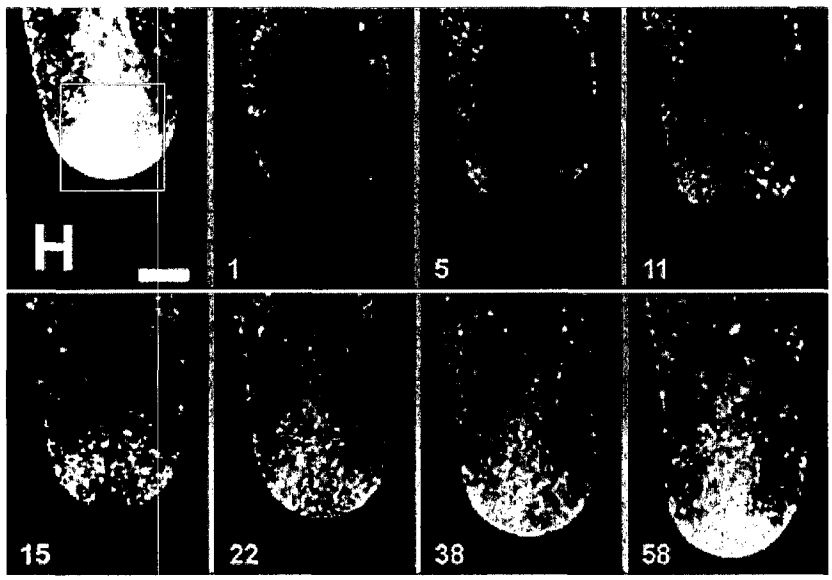

Figure 3.6: FRAP experiment. Image time series showing the recovery of fluorescence in the apical region (white square) after photobleaching, with time indicated in seconds. Fluorescence recovery starts from the shoulder of the region, evolving towards the center, then reaching the tip. Scale bar = 5 μm. Adapted from [23], with permission.

growth of 7 μm/min, they estimate that about 2.4×10^4 vesicles are needed to provide for cell wall expansion, while only 4×10^3 vesicles are needed for the expansion of the plasma membrane. This leaves about 2×10^4 vesicles which need to be delivered to the apex for cell wall exansion, but whose phospholipid bilayer membrane is not required for tube elongation. Two models are possible to explain this discrepancy: a "kiss-and-run" exocytosis by which the vesicle delivers its contents but escapes without fusing with the cell wall, or simply the formation of new vesicles from the apical membrane via endocytosis. Figure 3.7 shows a cartoon version of vesicle dynamics as hypothesized from available data in the current and past studies. Further experiments are needed to determine whether "kiss and run" or the endocytosis mechanism is used in plant cells.

The results in this chapter represent the first application of STICS for studies on plant cells (previous STICS work was done on cultured mammalian cells) and has been published [23]. In the next chapter, a new application of STICS to neuronal cells is presented.

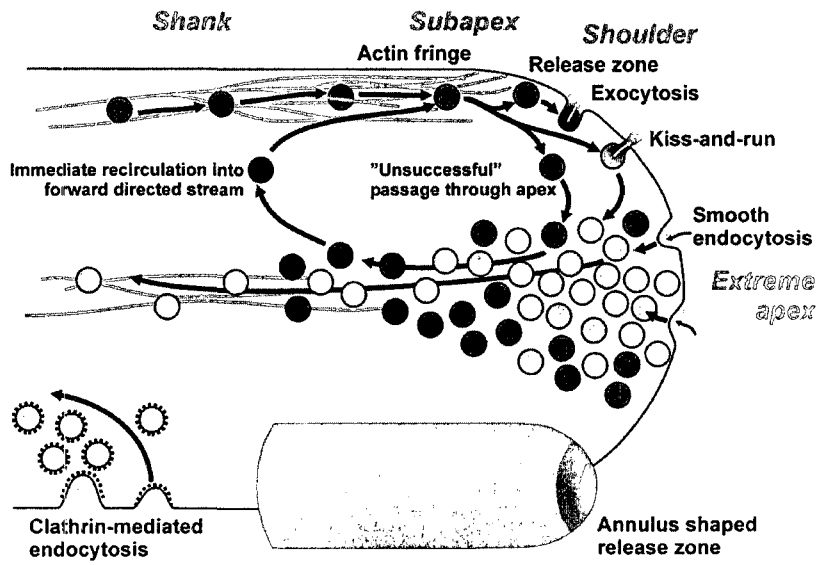

Figure 3.7: Schematic representation of vesicle dynamics inside growing pollen tubes. Vesicles travel along longitudinal actin filaments in the shank and into the subapical region, before being released in the shoulder of the tube. Under hydrodynamic force, some vesicles turn without contacting the plasma membrane, while others release their contents by a kiss-and-run mechanism or complete exocytosis, and new vesicles are formed by endocytosis of the outside medium. From [23].

Chapter 4

Actin dynamics in vertebrate growth cones

The second application of STICS presented in this work is the measurement of actin dynamics inside chick dorsal root ganglion (DRG) neuronal growth cones. This constitutes an experimental challenge because of the limited size of vertebrate growth cones, which usually range around 10 μm in size, and because the growth cones are very dynamic, constantly changing shape by extending and retracting long protrusions while migrating. The evolving boundaries limit the applicability of STICS to the central domain, due to problems in fitting the correlation functions because of edge effects [32]. However in the central domain the retrograde flow of actin can be mapped in both direction and speed by STICS analysis.

4.1 Materials and Methods

The neurons used for the study of growth cone actin dynamics were extracted from chick dorsal root ganglion (DRG) and cultivated in L15 medium (Invitrogen). They were then preplated on a glass substrate coated with 20 μg/mL of laminin, an extracellular matrix protein found outside the basement membrane of internal organs. The DRG were incubated in minimal medium for 30 minutes at 37 °C in an environmentally controlled chamber, after which they were transfered to a medium of F12 and E27 (Invitrogen), along with 50 ng/mL of nerve growth factor (NGF). The fluorescent marker (see below) was added at this point, with the help of a recombinant herpes simplex virus (HSV). The cells were incubated overnight and imaged the next

day. The time lapse image series were captured using a Zeiss Axiovert 200 widefield microscope with a 480/30 nm excitation from a Xenon lamp and 535/40 nm emission filter through a 505 nm long pass dichroic.

The fluorescent marking of F-actin (filamentous actin), as opposed to monomeric G-actin, is done by transfecting the neurons via a recombinant virus carrying DNA coding for utrophin (UTR), a protein that binds to F-actin, marked with GFP. To prepare the virual vector, GFP-UTR DNA plasmids are first injected into 2-2 cells (a derivative of african green monkey kidney cells, [41]), using lipofection. The cells were then infected with empty herpes simplex virus (HSV) [42] which also package the GFP-UTR DNA as they replicate inside the infected cells. The cells were then lysed and the defective virus particles harvested and reinjected into the neuronal growth medium, where they infected the neurons and injected the GFP-UTR DNA. The labeled utrophin is expressed by the neuron and binds to filamentous actin, serving as a probe for F-actin.

4.2 Results

Series of time lapse microscopy images were obtained for the migration of growth cones for living neurons cultivated in the laboratory. One of the challenges in applying STICS the DRG growth cones is that they are very small, being about 10 μm in diameter, limiting the STICS analysis to the central domain of the growth cone and to larger lamellipodia, away from the edges of the cell. Nonetheless, measurement of actin dynamics in the central domain is of crucial importance for the understanding of growth cone motility, since it is coupled with lamellipodia and filipodia formation in the peripheral region. Figure 4.1 shows the results of the STICS analysis on one growth cone. Previous applications of STICS selected regions of interest prior to analysis; however, since we are interested here in locating the central domain, we applied STICS blindly to the entire image, and applied a series of filters to the generated vector maps in order to include only the vectors of interest. This approach was necessary when the growth cones had a very irregular shape, and the postion of the central domain could not be infered from the geometry, but rather from the movement of actin as calculated in the analysis.

The image series was first analyzed using the STICS software over the entire field of view cropped around the growth cone. This yielded a vector map containing many edge effects, for vectors calculated over subregions that spanned across the edge of

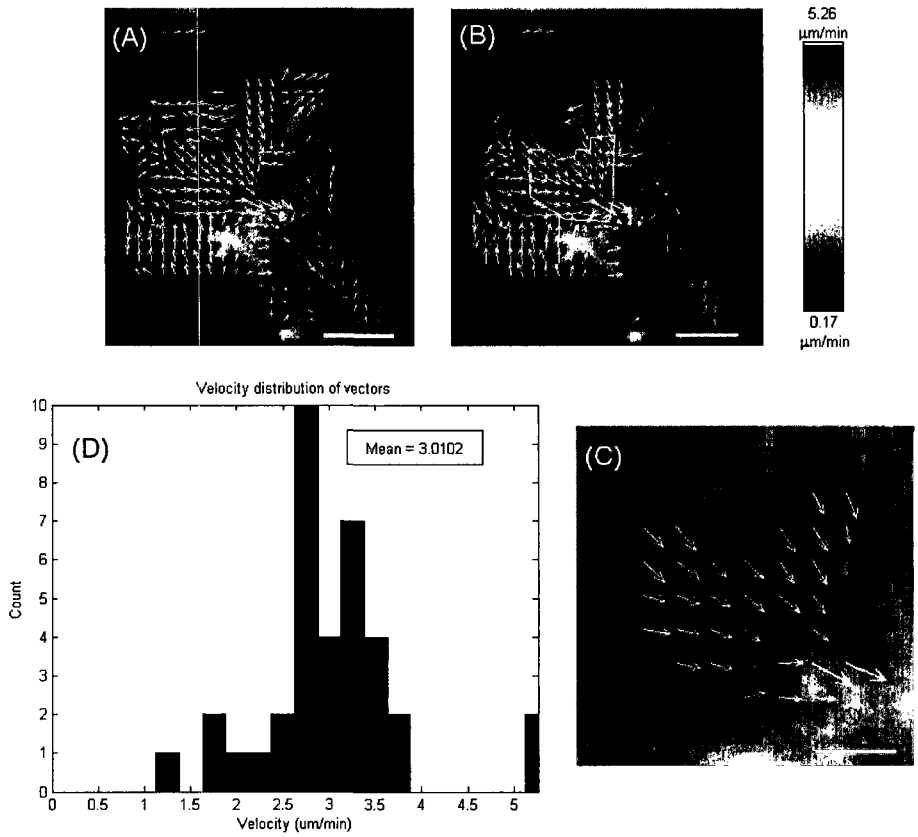

Figure 4.1: An overview of post-STICS treatment of vector map. (A) The raw vector map, as calculated with the STICS software over 16x16 pixels subregions and Fourier filtering, which includes many erroneous vectors due to edge effects. (B) The same vector map, filtered for directionality, with the central domain's centroid circled in red and the ROI highlighted as the polygon in white. (C) Vector map containing only the vectors in the ROI. (D) Histogram of speed distribution for vectors in the central domain. Scale bar in (A),(B) = 10 μm. Scale bar in (C) = 5 μm.

the growth cone. These vectors had a systematic error and were excluded from the results. The first step in post-STICS treatment was to manually define the centroid of the central domain, which was defined as the converging point of vectors within the bulk of the cone. This centroid was used to filter vectors with respect to their directionality (see Fig. 4.1(B)). Typically, every vector pointing more than 90° away from the centroid was removed. Then a region of interest was defined to surround vectors which lay within the central domain and far from the edge (typically more than 8 pixels away, considering 16x16 pixels subregions for each vector). Remaining

vectors represent the actin dynamics in the central domain, which can be used to assess the response of actin dynamics to external chemical stimuli which influence growth cone migration and the cytoskeleton.

4.2.1 Treatment with blebbistatin

To verify that STICS can measure differences in central domain actin dynamics, growth cones were treated with low concentrations of blebbistatin, which has previously been reported to reduce the central domain retrograde flow of actin in Aplysia growth cones [43, 44]. Blebbistatin blocks the effect of myosin II, a motor protein, by inhibiting the ATPase enzyme which drives the movement of myosin II along actin filaments. The growth cones were imaged before and after treatment in 70 μM blebbistatin, with a 5 to 10 minute interval between imaging to let the blebbistatin act. The effect on actin dynamics, and sometimes on the entire growth cone, is obvious, slowing down the formation of lamellipodia and filipodia, or completely killing the cell under high treatment concentrations. In some image series taken 5 minutes after treatment, the gradual breakdown of actin dynamics can be observed from the time the blebbistatin starts to act (see Figure 4.2).

Applying STICS on the central domain of growth cones before and after treatment with low concentrations of blebbistatin, we find that the flow after treatment only measures up to 0.6 ± 0.2 of the pre-treatment case ($n = 5$) (see Figure 4.3.(A)). Control experiments with DMSO (the blebbistatin solvent) do not show such reduction, yielding a 1.3 ± 0.2 ratio between the post- and pre-treatment measurements ($n = 4$) (Figure 4.3.(B)).

4.3 Discussion

F-actin polymerization and its movements are regulated by a complex array of proteins, the details of which are under active investigation (for a review, see [45]). These measurements provide strong evidence that the blebbistatin, which inhibits the activity of myosin II and the formation of actin bundles, not only reduces the formation of filipodia, but also affects the central domain retrograde flow of actin filaments, as it was reported for Aplysia growth cones in [44] and [46]. This constitutes the first measurement of actin retrograde flow for small vertebrate growth cones, which opens the door to a new range of biological questions concerning the role of F-actin in

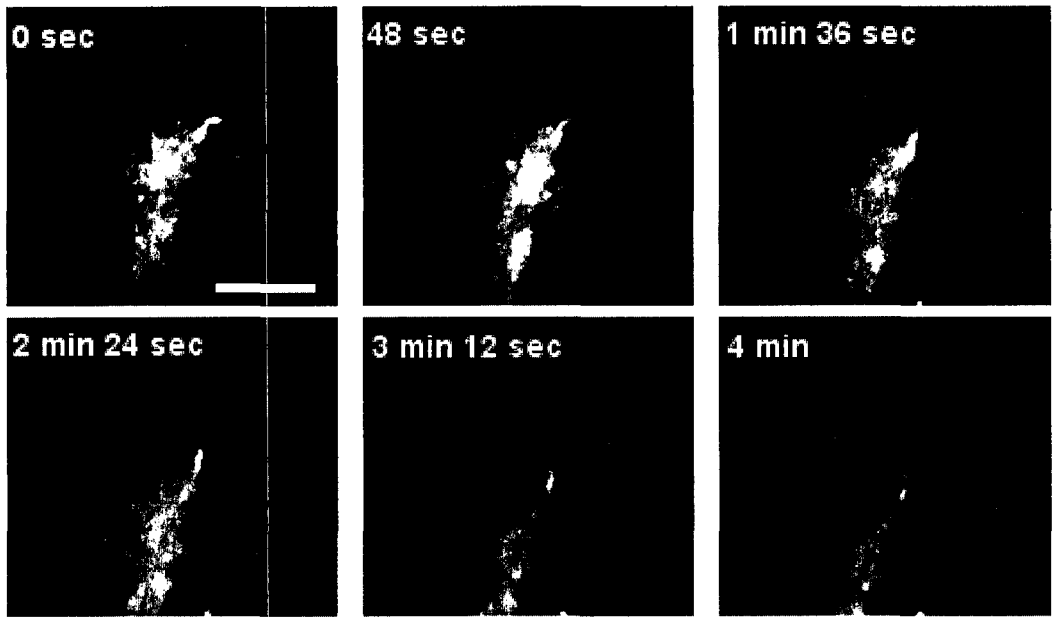

Figure 4.2: A growth cone at intervals of 48 seconds, with frame 0 sec recorded 5 minutes after the blebbistatin treatment. The filipodia gradually disappear and the cone loses most of its motility. Scale bar = 10 μm.

growth cone migration. Future studies to be conducted in continuation of this work will include the measurement of central domain F-actin response to guidance. Many publications have reported on the role of guidance cues such as netrin and Ca^{2+} ion gradients in axon guidance ([47, 48]). Using STICS, it will be possible to measure the asymmetric response and evolution of F-actin retrograde flow. The details of such analysis have not yet been settled, however a preliminary approach could consist in setting up a NGF gradient a right angle with axon orientation, and split the growth cone into near and far regions with respect to NGF concentration (see Figure 4.4).

The evolution of the central domain F-actin vectors under the influence of NGF can then be characterized by running STICS over subsequent time windows. The goal is to measure a link between growth cone turning and the response of F-actin in the central domain cytoskeleton. The experimental set up for this study is being done in collaboration with the Fournier lab at the Montreal Neurological Institute, and data should be available in the near future.

The results of this chapter serve as proof of principle that STICS can be used to measure the response of F-actin dynamics to molecular signals in vertebrate growth

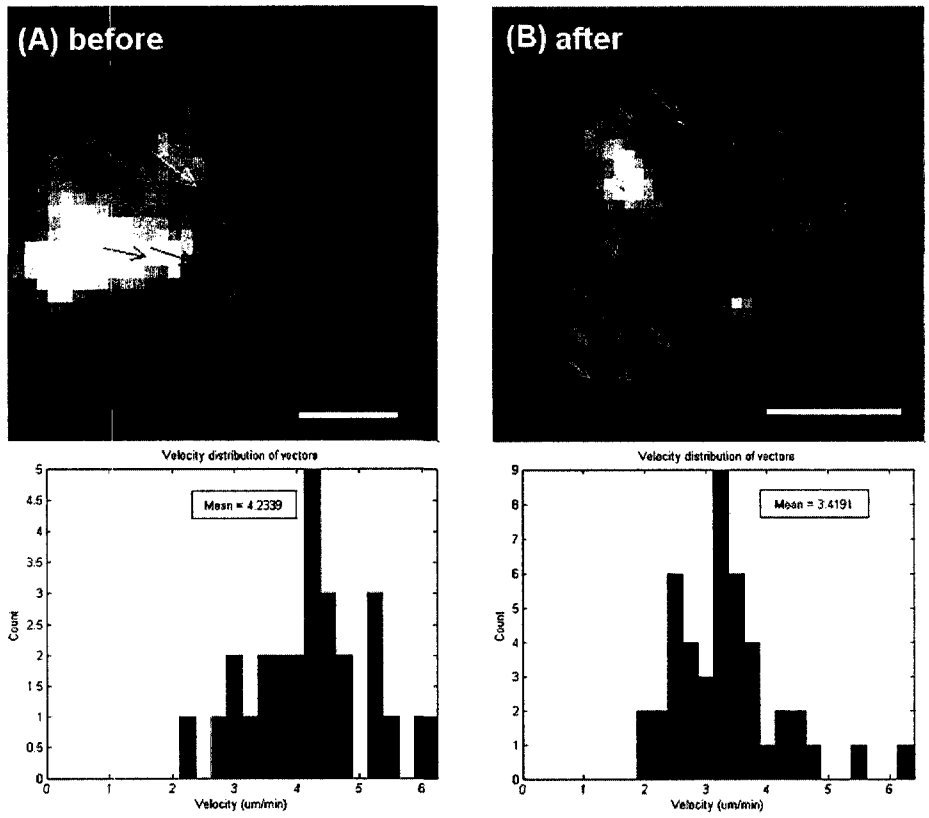

Figure 4.3: Example of vector maps and velocity histograms of a growth cone before (A) and after (B) treatment with blebbistatin. The average central domain F-actin flow speed drops to about 81% of its value. Scale bar (A) = 2 μm, scale bar (B) = 3 μm.

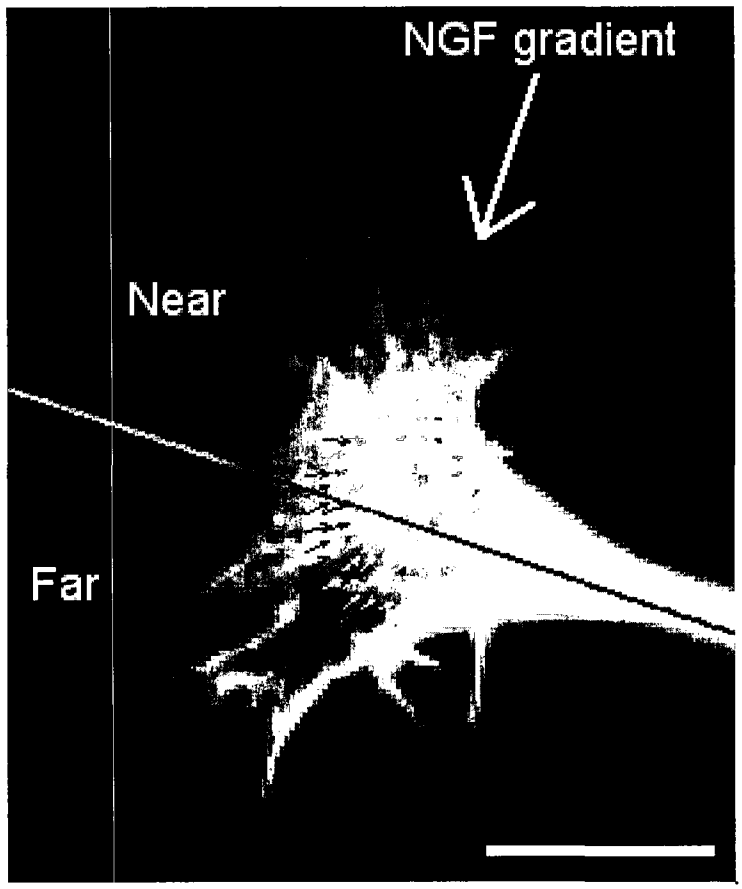

Figure 4.4: Preliminary approach for the measurement of growth cone F-actin response to guidance cues. The cone is split along its axis to define two distinct regions of analysis. The time evolution of actin retrograde flow in each region can then be characterized by using STICS over subsequent (perhaps overlapping) time frames. Scale bar = 10 μm.

cones. This application of the technique can provide new insight into the processes that regulate growth cone migration and dynamics of the cytoskeleton. As researchers in neuroscience continue to piece together the complex interactions involved in axon guidance and synapse formation, STICS can play a crucial role in providing a full understanding of the underlying dynamics and mechanisms of such biological phenomena.

Chapter 5

Conclusion and Outlook

Two new biological applications of spatiotemporal image correlation spectroscopy (STICS) were presented in this thesis. Chapter 3 described its use to measure the "cargo" vesicles inside growing pollen tubes of lily flowers. Very fast vesicle movements were measured, with speeds reaching 1.4 μm/s down the center and 0.7 μm/s up along the periphery. The results were consistant with the presence of an actin network carrying the vesicles forward along the tube's periphery and releasing them into the apex. The measured movement in the apex was also consistent with the observed formation of an inverted cone converging towards the center of the tube, with vesicles accelerating their way out of the apex and into the tube after diffusing somewhat freely in the apical region. The measurements have allowed to shed some light on the way the vesicles are transported in growing pollen tubes, as well as raising new questions about the processes by which they deliver their material to the apical membrane for the formation of the cell wall. Several possible mechanisms are suggested, including a kiss-and-run mechanism in which the vesicles make contact with the membrane and delivers its content, but does not fuse with the membrane. Such a process, combined with endocytosis through the tube's tip, can account for the discrepancy between the amount of plasma membrane gained from vesicles and the volume of cell wall material delivered by the latter. Further studies will be needed to assess which proportion of vesicles in the apex come from endocytosis and which are involved in a kiss-and-run mechanism.

The second application of STICS involved the measurement of F-actin dynamics in the central domain of chick DRG neuronal growth cones. Although the application is limited by the relatively small size of the growth cones and the need to exclude cell edges from the analysis, it is shown that STICS can be used to reliably measure

the response of central domain F-actin to external chemical cues such as blebbistatin. Future work will include the analysis of actin dynamics in response to attractive or repulsive stimuli. Most of the research efforts about axon guidance concentrate on the dynamics of filipodia to explain the process by which growth cones are directed along their path to form synapses. However, a study of the underlying actin dynamics will be necessary to provide a full understanding of the physical and chemical processes involved. As was shown, STICS can be used to answer some of these questions about underlying actin dynamics. Future approaches will have to include STICS in combination with other quantitative methods in order to trace the link between lamellipodia and filipodia activity and cytoskeletal actin dynamics. Traction force microscopy [49] and semi-automated filipodia tracking [50] are some of the techniques that may prove successful in probing filipodia activity.

Since its recent introduction to the field of biophysics, STICS has proven useful for applications in a wide variety of biological systems. Its ability to measure the flow of a fluorescent protein population, when a large fraction of the particles are immobile or slowly diffusing, makes it a powerful tool in the study of membrane and cytoskeletal protein dynamics, as well as dynamics of other intracellular structures, as was shown in this thesis. With powerful tools such as STICS, researchers from all fields can construct and test more quantitative biophysical models for complex biological systems, and keep looking further into the great mysteries of life.

Appendix A

Source code

This appendix contains the Matlab program used for the post-STICS treatment of vectors in the growth cone vector maps:

```
% This function isolates the central domain vectors of growth cone actin dynamics
% by using a directional filter and a manually defined ROI.
% Benoit Vaillancourt
% 2008-04-14

function centralDomainFinder()

%%  Input a STICS data file and corresponding image stack

    [filename pathname ] = uigetfile('*.mat','Select file to be
 analyzed','multiSelect','off');

    loadName = char(strcat(pathname,filename));
    data = load(loadName);
    velocityMap = data.velocityMap;
    settings = data.settings;

    [filename pathname ] = uigetfile('*.tif','Select corresponding image stack');

    stackName = strcat(pathname,filename);
    stack = readstack(stackName);
```

```
    firstImage = stack(:,:,35);

    gridIndexj = velocityMap.gridIndexj;
    gridIndexi = velocityMap.gridIndexi;
    angFilter = velocityMap.goodVectors;
    distFilter = velocityMap.goodVectors;
    goodVectors = velocityMap.goodVectors;
    Px = velocityMap.Px;
    Py = velocityMap.Py;

%%  Calculate the mean and median velocity
    average = mean(velocityMap.magnitudesPerMin);
    x = 0:0.25:max(velocityMap.magnitudesPerMin);

%%  Plot histogram

    plotHistograms(velocityMap.magnitudesPerMin, average);

    function plotHistograms(speedDist, mean)

        figure
        hist(speedDist,x)
        xlabel('Velocity (um/min)');
        ylabel('Count');
        title('Velocity distribution of vectors');
        set(gca,'XLim',[0 max(speedDist)]);

        anno = annotation('textbox',[0.6 0.8 0.18 0.07]);
        set(anno,'String',['Mean = ',num2str(mean)],'HorizontalAlignment',
  'center','VerticalAlignment','middle');
    end


%%  Prepare variables that might be used in plotting vector map
```

```
    minGlobalVel = nanmin([velocityMap.minVel]);
    maxGlobalVel = nanmax([velocityMap.maxVel]);

    colormapsize = 128;
    fullcolormap = colormap(jet(colormapsize));
    fullcolormap(end,:) = [1 1 1];
    fullcolormap(1,:) = [0 0 0];
    colormap(fullcolormap);

    fontWeight = 'normal';
    fontName = 'Arial';

%%  Draw the vector map and color bar

    % Plot only vector map and vertical color legend on the side,
    % no histogram

    h2a = figure;
    set(h2a,'InvertHardcopy','off','NumberTitle','off','Name','Vector Map and
 Scale Bar');

    % Plots vector maps and histograms
    axes('Position',[0 3/5 1 2/5])

    subplot(2,3,[1 5]);
    plotVelocityMap(settings, velocityMap, firstImage, 'Vector Map and Scale Bar')
    set(gcf,'Color','white')

    % Plots velocity scale bar
    subplot(2,3,[3 6]);

 subimage(ind2rgb(flipud(repmat(1:length(fullcolormap),
 length(fullcolormap),1)'),fullcolormap));
    set(gca,'XTick',[],'YTick',[]);
    daspect([10 1 1])
```

```
text(mean(get(gca,'XLim')),max(get(gca,'YLim')),
{[num2str(minGlobalVel,'%1.2f') ' ']};'\mum/min '},
'HorizontalAlignment','center','VerticalAlignment','top',
'FontWeight',fontWeight,'FontName',fontName)

text(mean(get(gca,'XLim')),min(get(gca,'YLim')),{['
'num2str(maxGlobalVel,'%1.2f')];' \mum/min'},'HorizontalAlignment','center',
'VerticalAlignment','bottom','FontWeight',fontWeight,'FontName',fontName)

   % Separately plot only the vector map, no scale bar
   h3 = figure;
   plotVelocityMap(settings, velocityMap, firstImage, 'Vector Map')
   set(h3,'InvertHardcopy','off','NumberTitle','off','Name','Vector Map');
   hold on

%% Call the centroidFinder function

   center = centroidFinder(firstImage);

%% Call the vectorAngleFilter and check if it's ok
   % Filter vectors using a specific angle threshold (pi/2) and replot

   angleInput = str2double(inputdlg('Enter angle (degrees)','Enter angle
threshold value',1,{'90'}));
   angleThreshold = angleInput*pi/180;

   vectorAngleFilter(center, angleThreshold)
   h4 = figure;
   plotVelocityMap(settings, velocityMap, firstImage, 'Vector Map')
   set(h4,'InvertHardcopy','off','NumberTitle','off','Name','Vector Map');
   hold on
   plot(center(1),center(2),'Marker','o','MarkerSize',12,'MarkerEdgeColor','r')

   ok = false;
```

```
    while ~ok
        threshCheck = questdlg('Is this ok?','Check','Yes','Change threshold
  value','Yes');
        if strcmp(threshCheck, 'Change threshold value')
            velocityMap.goodVectors = goodVectors;
            plotVelocityMap(settings, velocityMap, firstImage, 'Vector Map')
            hold on
            plot(center(1),center(2),'Marker','o',
'MarkerSize',12,'MarkerEdgeColor','r')

            newAngle = str2double(inputdlg('Enter new angle (degrees)','Change
   angle threshold value',1));
            angleThreshold = newAngle*pi/180; % Change to radians
            vectorAngleFilter(center, angleThreshold)
            plotVelocityMap(settings, velocityMap, firstImage, 'Vector Map')
            set(h4,'InvertHardcopy','off','NumberTitle','off','Name',
'Vector Map');
            hold on

plot(center(1),center(2),'Marker','o','MarkerSize',12,
   'MarkerEdgeColor','r')
        else
            ok = true;
        end
    end
    velocityMap.goodVectors = angFilter;
    distFilter = angFilter;
    filter = logical(zeros(size(angFilter)));

%% Select ROI

    [ROImask, maskX, maskY] = roipoly();

    % deletes old ROI region if present on axis
```

```
    maskOutline = line(maskX,maskY,'Color','w','LineWidth',1);
    drawnow;
    % Make a filter vector based on the ROImask
    for k = 1:length(angFilter)
        if (ROImask(gridIndexi(k),gridIndexj(k)) && angFilter(k) )
            filter(k) = 1;
        end
    end

    velocityMap.goodVectors = logical(filter);

    h6 = figure;
    plotVelocityMap(settings, velocityMap, firstImage, 'Vector Map')
    set(h6,'InvertHardcopy','off','NumberTitle','off','Name','Vector Map');
    hold on
    plot(center(1),center(2),'Marker','o','MarkerSize',12,'MarkerEdgeColor','r')

%% Plot new histogram with average speed

    magnitudesPerMin = sqrt(Px(filter,2).^2 + Py(filter,2).^2)*60;
    average = mean(magnitudesPerMin);
    plotHistograms(magnitudesPerMin, average);

%% Angle filter
    function vectorAngleFilter(center, angleThreshold)
    % This functions takes in x-y coordinates and a velocityMap data structure
    % and filters the vectors with respect to their orientation.

        for i = 1:length(angFilter)
            if  goodVectors(i)
                refVector = [gridIndexj(i) - center(1), gridIndexi(i) -
 center(2)];
                mapVector = [Px(i,2); Py(i,2)];
                angle = acos((refVector*mapVector)/(sqrt(refVector(1)^2 +
 refVector(2)^2)*sqrt(mapVector(1)^2 + mapVector(2)^2) ));
```

```
                if angle > angleThreshold
                    angFilter(i) = 0;
                end
            end
        end
        velocityMap.goodVectors = angFilter;
    end

%% Distance filter
    % Filters vectors according to their distance from the centroid

    function vectorDistFilter(center, radius)

        for i = 1:length(distFilter)
            if distFilter(i)
                vectorDist = sqrt( (center(1)-gridIndexj(i))^2 +
      (center(2)-gridIndexi(i))^2 );
                if vectorDist > radius
                    distFilter(i) = 0;
                end
            end
        end
        velocityMap.goodVectors = distFilter;
    end

%% Position filter
    % Filters according to their position wrt lines 1 and 2

    function vectorPosFilter(deltaTheta)

        for i = 1:length(distFilter)
            if distFilter(i)

                phi1 = acos(((gridIndexj(i)-center(1))*line1vec(1) +
                (gridIndexi(i)-center(2))*line1vec(2))/(sqrt((center(1)-
```

```
gridIndexj(i))^2 +
(center(2)-gridIndexi(i))^2)*sqrt(line1vec(1)^2+line1vec(2)^2)) );

phi2 = acos(((gridIndexj(i)-center(1))*line2vec(1) +
(gridIndexi(i)-center(2))*line2vec(2))/(sqrt((center(1)-
gridIndexj(i))^2 +
(center(2)-gridIndexi(i))^2)*sqrt(line2vec(1)^2+line2vec(2)^2)) );

                if phi1 > deltaTheta || phi2 > deltaTheta
                    distFilter(i) = 0;
                end
            end
        end
        velocityMap.goodVectors = distFilter;
    end
end
```

Bibliography

[1] Benedict Hebert, Santiago Costantino, and Paul W. Wiseman. Spatiotemporal image correlation spectropscopy (STICS) theory, verification, and application to protein velocity mapping in living CHO cells. *Biophysical Journal*, 88:3601–3614, 2005.

[2] Benedict Hebert. *Spatio-temporal Image Correlation Spectroscopy: Development and Implementation in Living Cells.* PhD thesis, Physics Department, McGill University, 2006.

[3] C. M. Brown, B. Hebert, D. L. Kolin, J. Zareno, L. Whitmore, A. R. Horwitz, and P. W. Wiseman. Probing the integrin-actin linkage using high-resolution protein velocity mapping. *Journal of Cell Science*, 119:5204–5214, 2006.

[4] O. Shimomura, F. H. Johnson, and Y. Saiga. Extraction, purification and properties of aequorin, a bioluminescent protein from the luminous hydromedusan, aequorea. *J. Cell. Comp. Physiol.*, 59, 1962.

[5] Joseph R. Lakowicz. *Principles of Fluorescence Microscopy*, chapter 1. Introduction to Fluorescence, pages 1–26. Springer Science + Business Media, third edition edition, 2006.

[6] A. Jablstrokonacuteski. ber den mechanismus der photolumineszenz von farbstoffphosphoren. *Zeitschrift fr Physik A Hadrons and Nuclei*, 94:38–46, 1935.

[7] P. L. Fegner, T. R. Gadek, M. Holm, R. Roman, H. W. Chan, M. Wenz, J. P. Northrop, G. M. Ringold, and M. Danielsen. Lipofection: A highly efficient, lipid-mediated DNA-transfection procedure. *PNAS*, 84:7413–7417, 1987.

[8] Philip Washbourne and A. Kimberley McAllister. Tehniques for gene transfer into neurons. *Current Opinion in Neurobiology*, 12:566–573, 2002.

[9] M. Minsky. Confocal microscope. *Microscopy Apparatus*, US Patent 3,013,467, 1961.

[10] W. B. Amos and J. G. White. How the confoacl laser scanning microscope entered biological research. *Biology of the Cell*, 95:335–342, 2003.

[11] G. J. Brakenhoff, H. T. M. van der Voort, E. A. van Spronsen, W. A. M. Linnemans, and N. Nanninga. Three-dimensional chromatin distribution in neuroblastoma cell nuclei shown by confocal scanning laser microscopy. *Nature*, 317:748–749, 1985.

[12] J. Heslop-Harrison. Pollen germination and pollen-tube growth. *International Review of Cytology*, 107:1–78, 1987.

[13] A. Geitmann and R. Palanivelu. Fertilization requires communication: Signal generation and perception during pollen tube guidance. *Floriculture and Ornamental Biology*, 1:77–89, 2007.

[14] K. L. Wilsen and P. K. Hepler. Sperm delivery in flowering plants. *BioScience*, 57:835–844, 2007.

[15] Y. Chebli and A. Geitmann. Mechanical principles governing pollen tube growth. *Functional Plant Sciences and Biotechnology*, 1:232–245, 2007.

[16] A. Moscatelli and M. Cresti G. Cai. Pollen and the pollen tube cytoskeleton. *Cell Biology International*, 21:883–885, 1997.

[17] G. Cai, A. Del Casino, S. Romagnoli, and M. Cresti. Pollen cytoskeletonduring germination and pollen tube growth. *Current Science*, 89:1853–1860, 2005.

[18] E. Yokota and T. Shimmen. *The actin cytoskeleton in pollen tubes actin and actin binding proteins*, volume 3 of *Plant Cell Monographs*, chapter The pollen tube: a cellular and molecular perspective, pages 139–155. Springer Verlag, Berlin Heidelberg, 2006.

[19] S. Romagnoli, G. Cai, C. Faleri, E. Yokota, T. Shimmen, and M. Cresti. Microtubule- and actin filament-dependent motors are distributed on pollen tube mitochondria and contribute differently to their movement. *Plant Cell Physiology*, 48:345–361, 2007.

[20] Y. Iwanami. Protoplasmic movement in pollen grains and tubes. *Phytomorphology*, 6:288–295, 1956.

[21] A. Lovy-Wheeler, K. L. Wilsen, T. I. Baskin, and P. K. Hepler. Enhanced fixation reveals the apical cortical fringe of actin filaments as a consistent feature of the pollen tube. *Planta*, 221:95–104, 2005.

[22] X. Wang, Y. Teng, Q. Wang, X. Li, X. Sheng, M. Zheng, J. Samaj, F. Baluska, and J. Lin. Imaging of dynamic secretory vesicles in living pollen tubes of *Picea meyeri* using evanescent wave microscopy. *Plant Physiology*, 141:1591–1603, 2006.

[23] Jerome Bove, Benoit Vaillancourt, Jens Kroeger, Peter K. Hepler, Paul W. Wiseman, and Anja Geitmann. Magnitude and direction of vesicle dynamics in growing pollen tubes using spatiotemporal image correlation spectroscopy (STICS) and fluorescence recovery after photobleaching (FRAP). *Plant Physiology*, 147(4):1646–58, 2008.

[24] R. G. Harrison. The outgrowth of the nerve fiber as a mode of protoplasmic movement. *Journal of Experimental Zoology*, 9:787–848, 1910.

[25] S. C. Landis. Neuronal growth cones. *Annual Review of Physiology*, 45:567–580, 1983.

[26] Anne K. Mongiu, Elizabeth L. Weitzke, Oleg Y. Chaga, and Gary G. Borisy. Kinetic-structural analysis of neuronal growth cone. *Journal of Cell Science*, 120:1113–1125, 2007.

[27] F. van den Ent, L. A. Amos, and J. Lowe. Prokaryotic origin of the actin cytoskeleton. *Nature*, 413:39–44, 2001.

[28] F. B. Straub. Actin. *Stud. Inst. Med. Chem.*, 2:3–15, 1942.

[29] D. Bray and K. Chapman. Analysis of microspike movements on the neuronal growth cone. *Journal of Neuroscience*, 5:3204–3213, 1985.

[30] E. W. Dent and F. B. Gertler. Cytoskeletal dynamics and transport in growth cone motility and axon guidance. *Neuron*, 40:209–227, 2003.

[31] S. J. Smith. Neuronal cytomechanics: the actin-based motility of growth cones. *Science*, 242:708–715, 1988.

[32] David L. Kolin and Paul W. Wiseman. Advances in image correlation spectroscopy: Measuring number densities, aggregation states, and dynamics of fluorescently labeled macromolecules in cells. *Cell Biochem. Biophys.*, 49(3):141–164, 2007.

[33] N. O. Petersen, P. L. Hddelius, P. W. Wiseman, O. Seger, and K.-E. Magnusson. Quantitation of membrane receptor distributions by image correlation spectroscopy: concept and application. *Biophysical Journal*, 65:1135–1146, 1993.

[34] Paul W. Wiseman and Nils O. Petersen. Image correlation spectroscopy. II. optimization for ultrasensitive detection of preexisting platelet-derived growth factor-β receptor oligomer on intact cells. *Biophysical Journal*, 76:963–977, 1999.

[35] E. L. Elson and D. Magde. Fluorescence correlation spectroscopy. I. conceptual basis and theory. *Biopolymers*, 13:1–27, 1974.

[36] D. Magde, W. W. Webb, and E. L. Elson. Fluorescence correlation spectroscopy. III. uniform translation and laminar flow. *Biopolymers*, 17:361–376, 1978.

[37] S. Costantino, J. W. D. Comeau, D. L. Kolin, and P. W. Wiseman. Accuracy and dynamic range of spatial image correlation and cross-correlation spectroscopy. *Biophysical Journal*, 89:1251–1260, 2005.

[38] D. L. Kolin, S. Costantino, and P. W. Wiseman. Sampling effects, noise, and photobleaching in temporal image correlation spectroscopy. *Biophysical Journal*, 90(2):628–639, 2006.

[39] A. Lovy-Wheeler, L. Cardenas, J. G. Kunkel, and P. K. Hepler. Differential organelle movement on the actin cytoskeleton in lily pollen tubes. *Cell Motility and the Cytoskeleton*, 64:217–232, 2007.

[40] M. Edidin, Y Zagyansky, and T. J. Lardner. Measurement of membrane lateral diffusion in single cells. *Science*, 191:466–468, 1976.

[41] I. L. Smith, M. A. Hardwicke, and R. M. Sandri-Goldin. Evidence that the herpes simplex virus immediate-early protein icp27 acts posttranscriptionally during transfection to regulate gene expression. *Virology*, 186:74–86, 1992.

[42] Cornal Fraefel. Gene delivery using helper virus-free hsv-1 amplicon vectors. *Current Protocols in Neuroscience*, 40:4.14.1 – 4.14.21, 2007.

[43] Nelson A. Medeiros, Dylan T. Burnette, and Paul Forscher. Myosin ii functions in actin-bundle turnover in neuronal growth cones. *Nature Cell Biology*, 8:216–226, 2006.

[44] Dylan T. Burnette, Andrew W. Schaefer, Gaudenz Danuser Lin Ji, and Paul Forscher. Filipodial actin bundles are not necessary for microtubule advance into the peripheral domain of aplysia neuronal growth cones. *Nature Cell Biology*, 9:1360–1369, 2007.

[45] Stephanie L. Gupton and Frank B. Gertler. Filipodia: The fingers that do the walking. *Sci. STKE*, 400, 2007.

[46] Michael W. Baker and Eduardo R. Macagno. In vivo imaging of growth cone and filipodial dynamics: Evidence for contact-mediated retraction of filipodia leading to the tiling of sibling processes. *Journal of Comparative Neurology*, 500:850–862, 2007.

[47]

[48] Jennifer Round and Elke Stein. Netrin signaling leading to directed growth cone steering. *Current Opinion in Neurobiology*, 17:15–21, 2007.

[49] Steven Munevar, Yu-Li Wang, and Micah Dembodagger. Traction force microscopy of migrating normal and H-ras transformed 3T3 fibroblasts. *Biophysical Journal*, 80:1744–1757, 2001.

[50] S. Costantino, C. B. Kent, A. G. Godin, T. E. Kennedy, P. W. Wiseman, and A. E. Fournier. Semi-automated quantification of filipodial dynamics. *Journal of Neuroscience Methods*, 171:165–173, 2008.